
GANSim-surrogate: An integrated framework for conditional geomodelling and uncertainty analysis

Suihong Song[1], Dongxiao Zhang[2,*], Tapan Mukerji[3], and Nanzhe Wang[4]

[1] Department of Mathematics and Theories, Peng Cheng Laboratory, Shenzhen 518000, China

[2] School of Environmental Science and Engineering, Southern University of Science and Technology, Shenzhen 518055, China

[3] Stanford University, 367 Panama St, Stanford, CA 94305, USA

[4] BIC-ESAT, ERE, and SKLTCS, College of Engineering, Peking University, Beijing 100871, China

Corresponding author: Dongxiao Zhang (zhangdx@sustech.edu.cn)

Abstract

We propose a deep-learning framework (GANSim-surrogate) for conditioning subsurface geomodel realizations to static data and dynamic flow data. The static data includes well facies data, interpreted facies probability maps, and non-spatial global features, while dynamic data can include well data such as pressures and flow rates. The framework consists of a Convolutional Neural Network (CNN) generator trained from GANSim (a Generative Adversarial Network-based geomodelling simulation approach), a CNN-based surrogate, and options for searching appropriate input latent vectors for the generator. The four search methods investigated are Markov Chain Monte Carlo, Iterative Ensemble Smoother, gradient descent, and gradual deformation. The framework is validated by applying it for geomodelling of channelized reservoirs. First, a generator is trained using GANSim to generate geologic facies models; in addition, a flow simulation surrogate is trained using a physics-informed approach. Then, given well facies data, facies probability maps, global facies proportions, and dynamic bottomhole pressure data (BHP), the trained generator takes the first three conditioning data and a latent vector as inputs and produces a random realistic facies model conditioned to the static data. To condition to the dynamic data, the produced facies model is converted to permeabilities and mapped to BHP data by the trained physics-informed surrogate. Finally, the mismatch between the surrogate-produced and the observed BHP data is minimized to obtain appropriate input latent vectors for the generator. The framework is computationally efficient, and the posterior facies models prove to be realistic and consistent with all of the conditioning data.

Key Words:

GANSim, geomodelling, uncertainty quantification, surrogate, Generative Adversarial Networks (GANs), Convolutional Neural Networks (CNNs), Physics-informed neural networks (PINNs)

Key Points:

- GANSim, a CNN-based surrogate, and search algorithms are combined for conditioning geomodels to static, dynamic, and geophysical data.
- A CNN-based flow surrogate for channel reservoirs is trained using physics-informed method (PINNs).
- Experiments prove that, the framework is fast, and its produced geomodels are realistic and consistent with all given conditioning data.

1 Introduction

Geomodelling, i.e., characterizing spatial distribution of subsurface reservoirs, is of great significance for the exploitation of underground water and hydrocarbon resources and the geological storage of CO_2. However, the perpetual issue of insufficient data and knowledge about the subsurface leads to great uncertainty in geomodelling of the reservoir distribution. Such uncertainty can be further transmitted into reserve evaluation, well production prediction, determination of new well locations, etc.

To decrease the uncertainty, as many types of information as possible about the subsurface reservoir should be integrated into the geomodelling process. Various types of information commonly include spatial geological structures or patterns, global features (e.g., facies proportion), well facies data (i.e., facies type at well locations), geophysical data, and temporal dynamic data observed at wells (e.g., daily measurements of bottomhole pressure). These types of information are presented in different forms and relate to reservoirs through different ways. (1) High-resolution well facies data are direct representation of reservoirs, yet very sparse in geological space. (2) Geophysical data covers the complete three-dimensional geo-space of subsurface reservoirs but is subject to limited resolution, fidelity, and complicated relationship with reservoir properties (e.g., porosity). It relates to reservoir properties through a rock physics model linking reservoir properties with rock properties (e.g., acoustic velocity) and a partial differential equations (PDEs)-dominated process taking rock properties into geophysical data (Bosch et al., 2010). (3) As a type of spatiotemporal data, dynamic data relates to reservoir properties also through a PDEs-dominated process that governs fluid flow. (4) Geological patterns describe the shapes and contact relations of different reservoir facies types. There is no mathematical expression of complete geological patterns, although the 3-D variogram function as a relaxed 2-point statistics approximation, object-based methods, spatial Markov random fields, process-mimicking algorithms, and training images implicitly capturing multiple-point spatial statistics are used to partially represent it in many cases (Deutsch, 2002; Mariethoz & Caers, 2014). (5) Global features, as scalars, describe the non-spatial global geometrical or quantitative features of reservoirs, such as the facies proportion, channel width, channel sinuosity, etc.

Traditionally, geostatistical approaches are used to integrate partial geological patterns and well facies data to simulate multiple reservoir realizations, e.g., variogram-based or multiple point statistics (MPS)-based methods (Deutsch, 2002; Mariethoz & Caers, 2014). To further condition to measured dynamic flow data, the above simulation process is perturbed to search for appropriate realizations that are not only conditioned to the given well facies data and partial geological patterns but are also consistent with the measured dynamic data through a simulator capable of flow simulation (see e.g., Caers, 2003a). Such a process centered on historical dynamic data is also called history matching. In recent decades, various aspects of history matching have been explored, including perturbation methods of the sequential simulation process (Caers, 2003a, 2003b; Hu et al., 2001), development of surrogate-based simulators (e.g., the polynomial chaos expansion surrogate proposed by Li & Zhang (2009)), and search methods for appropriate realizations (e.g., gradual deformation (Caers, 2003a; Hu, 2000), probability perturbation methods (Caers & Hoffman, 2006; Hu, 2008), probability conditioning methods (Jafarpour & Khodabakhshi, 2011), ensemble-based methods (Chang et al., 2017; Chen & Oliver, 2013), and Markov Chain Monte Carlo (MCMC)-based methods (Efendiev et al., 2015; Liao et al., 2019; Ma et al., 2008)). Two approaches have been used to condition reservoir simulations to

geophysical data: joint inversion and sequential inversion. The joint inversion process is very similar to history matching, except a rock physics model is inserted to transform simulated reservoir realizations into physical properties which are then used to forward simulate geophysical data. In sequential inversion, probability maps of different reservoir facies types are first obtained using for example statistical rock physics and quantitative interpretation workflows (e.g. Avseth et al. (2005)); then these probability maps are taken as soft constraining data in geostatistical simulation approaches to produce reservoir realizations. Bosch et al., (2010) gives a review of both workflows.

Through all the above processes, the produced reservoir realizations can honor the given global features, well facies data, dynamic data, geophysical data, and expected geological patterns to some extent. However, the variograms or multiple points statistics of a training image can only partially represent the complicated geological patterns, thus there is a lack of realism in the simulated reservoir realizations, to different extents, e.g., discontinuous channels produced by MPS-based methods. Additionally, traditional simulators applied in history matching and geophysical inversion processes are relatively slow compared to the requirement of a large number of simulator iterations in the two processes, making it computationally expensive to achieve conditioning of the produced reservoir realizations to the given geophysical and dynamic data in practice.

Generative Adversarial Networks (GANs; Goodfellow et al., 2014) in deep learning can capture complicated spatial patterns of 2D images or 3D objects using a generator composed of Convolutional Neural Networks (CNNs). With the captured pattern knowledge, the generator can produce realistic images or 3D objects from low-dimensional latent vectors (Wu et al., 2016). Researchers combined GANs with geomodelling on different aspects (Chan & Elsheikh, 2017, 2019; Dupont et al., 2018; Laloy et al., 2018; Mosser et al., 2020; Nesvold & Mukerji, 2021; Song et al., 2021a, 2021b, 2022a, 2022b; Zhang et al., 2019). For unconditional geomodelling, the generator of GANs is first trained to learn geological patterns from a training set of many conceptual facies models; then, with the learned geological patterns, the generator can quickly map random latent vectors into multiple realistic reservoir realizations, see e.g., Song et al. (2021a). To achieve conditioning, appropriate latent vectors are searched so that they can be mapped by the trained generator into realizations that are consistent with the given conditioning data (Laloy et al., 2018, 2019; Mosser et al., 2020; Nesvold & Mukerji, 2021; Zhang et al., 2019). This process is similar to history matching and geophysical inversion, except the original geostatistical simulation process of facies models is replaced by the trained generator. Various latent vector search approaches (e.g., gradient descent, gradual deformation, ensemble methods, and MCMC methods) can be used here.

Recently, Song et al. (2021b, 2022a) proposed a new GANs-based workflow for direct conditional geomodelling, called GANSim, where the trained generator takes the given global feature values, well facies data, geophysics-interpreted facies probability maps, and random latent vectors as inputs and directly produces various realistic reservoir realizations consistent with all of the input conditioning data. There is no need for an expensive latent vector search process in GANSim. Song et al. (2022b) applied GANSim for uncertainty geomodelling of 3D karst cave field reservoirs conditioned to well facies data and 3D facies probability cubes interpreted from seismic data, with excellent performance. However, GANSim cannot achieve direct conditioning to the original geophysical data and dynamic data, in which case, the latent vector search process may still be needed to be combined. However, compared to using the

trained unconditional generator (i.e., generator only taking a latent vector as input) for the latent vector search process, here with the trained conditional generator of GANSim, the computational resources and time required by the search process should be largely reduced, because the appropriate latent vectors only need to be consistent with the geophysical or dynamic data instead of all the given conditioning data types.

Forward simulators are required in all forms of history matching and geophysical inversion processes including the aforementioned ones involving trained generators. To improve the running speed of simulators, CNN-based surrogates are largely studied using either data-driven (Tang et al., 2021) or physics-informed (e.g., Wang et al., 2021; Xu et al., 2022) approaches. The data driven approach enables the learning of PDE-dominated relationships between geophysical/dynamic data and rock/reservoir properties from training input-output labelled data pairs, while the physics-informed approach (i.e., Physics-informed Neural Networks (PINNs); Karniadakis et al., 2021), enforces CNNs to directly learn knowledge from PDEs. Indeed, the CNN-based surrogate is relatively easy to train with data-driven method, but the trained surrogate may violate physics locally. In contrast, physics-informed training is slow and may involve problems like tunning of weight hyperparameters but ensures consistency with physics constraints and does not require a great many of input-output labelled data pairs for training. Wang et al. (2021) proves largely improved accuracy of physics-informed approach compared to purely data-driven approach and reduced running time of the CNN-based flow surrogate compared to a traditional finite difference-based simulator, MODFLOW.

Mo et al. (2020) proposed to combine variational auto-encoder, another type of generative model comparable to GANs, a CNN-based surrogate, and Iterative Ensemble Smoother for geomodelling conditioned to dynamic flow data, but the well facies data, global features, and probability maps are not honored. Additionally conditioning to these types of data may be achieved by a more elaborate latent vector search process but takes longer time.

In this paper, we propose the GANSim-surrogate framework, by combining GANSim and CNN-based surrogate together, to quickly produce reservoir realizations that are consistent with expected geological patterns as well as the given global features, well facies data, geophysical data or its interpreted facies probability maps, and dynamic flow data. Section 2 introduces the general GANSim-surrogate framework. Then, to showcase the procedures of this framework and validate its effectiveness, we apply this framework for uncertainty geomodelling of channel reservoirs. In section 3, we concretize the framework by constructing a generator and a surrogate specifically for channel reservoirs. In section 4, the concretized GANSim-surrogate framework is used for uncertainty geomodelling of channel reservoirs in two test cases conditioned to given facies proportion value (as a type of global feature), well facies data, geophysics-interpreted probability map, and dynamic data. Finally, sections 5 and 6 give discussions and conclusions of this study, respectively.

2. GANSim-surrogate framework

In this section, first we present the general workflow of GANSim-surrogate framework, then three important components of this workflow are described.

2.1 General GANSim-surrogate workflow

The proposed GANSim-surrogate framework is illustrated as in Figure 1. For a specific class of reservoir, the first step of the framework is to train a CNN-based generator using the

standard GANSim approach (described in section 2.2 briefly and Appendix A in detail) and a CNN-based surrogate using either the data-driven or the physics-informed approach (described in sections 2.2 and 3.2) for this reservoir class. The trained generator can then take well facies data, global features, facies probability maps, and a latent vector as inputs and produce a random reservoir facies model that is consistent with the three types of input conditioning data as well as the expected geological patterns of the reservoir class of interest. As a substitution of the forward simulator involved in history matching or geophysical inversion, the trained surrogate can map reservoir properties (e.g., permeability distribution) into dynamic data (in history matching process) or map rock properties (e.g., acoustic velocity) into geophysical data (in geophysical inversion process).

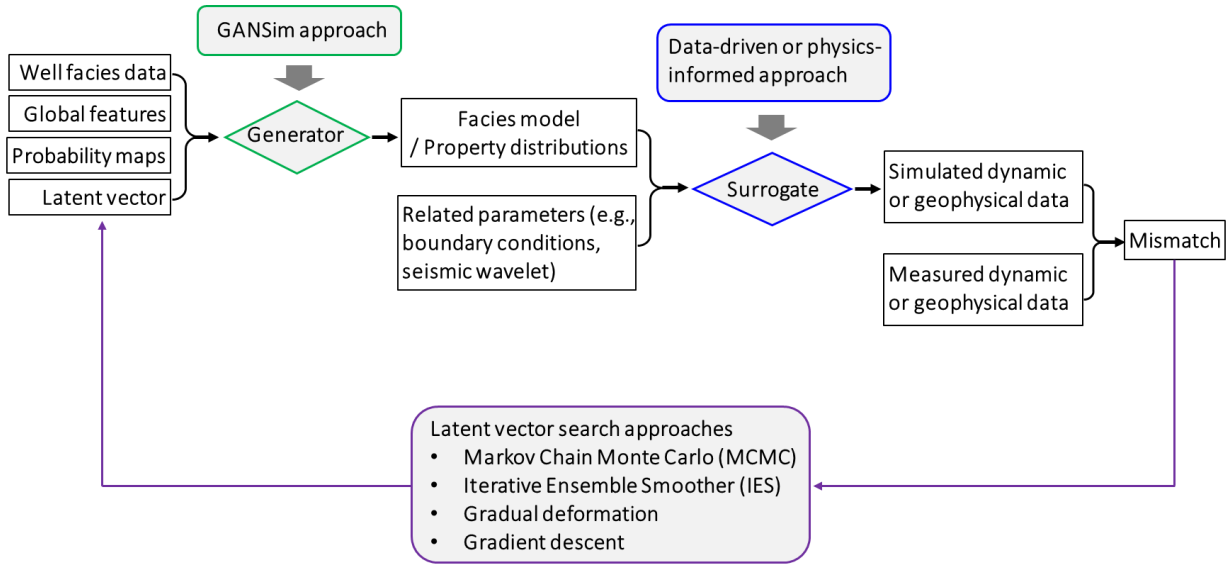

Figure 1. General workflow of GANSim-surrogate framework.

For a new reservoir from the interested reservoir class, given its well facies, global feature values, facies probability maps, original geophysical data, and dynamic data as conditioning data, first, the trained generator takes the given well facies data, global features, probability maps, and random latent vectors as inputs and produces multiple realistic and conditional facies model realizations. Second, these realizations are transformed into reservoir property distributions with geostatistical approaches (in history matching) or rock property distributions with rock physics models (in geophysical inversion). Next, the trained surrogate takes the transformed reservoir/rock property distributions and other related parameters (e.g., initial and boundary conditions, seismic wavelet) as inputs and produces dynamic/geophysical data. Then, the mismatch between the produced dynamic/geophysical data and the field measured one is minimized by perturbing and searching for appropriate latent vectors. Four latent vector search approaches are investigated here, viz., MCMC, Iterative Ensemble Smoother (IES), gradient descent, and gradual deformation. Appendix B gives a brief description of these search approaches used in this paper. Finally, the pretrained generator takes as inputs these appropriate latent vectors as well as the given well facies data, global features, and probability maps, and produces different facies model realizations that are consistent with the expected

geological patterns, the three types of input conditioning data, as well as the field-measured dynamic or geophysical data.

Once the generator and the surrogate are trained, this workflow is computationally very fast for uncertainty geomodelling. Note that the three types of input conditioning data are not necessarily all needed as inputs of the generator.

2.2 Components of GANSim-surrogate framework

(1) GANSim

Based on GANs, GANSim (Song et al., 2021b, 2022a) aims at training a CNN-based generator which takes as inputs various types of conditioning data as wells as a latent vector and produces facies model realizations that are consistent with the expected geological patterns and the input conditioning data. Different input latent vectors generate different facies realizations. Compared to the conventional GANs-based unconditional geomodelling workflow (e.g., Song et al., (2021a), in GANSim, the architecture of the generator is improved to take different types of conditioning data as inputs, and an additional type of loss function, called condition-based loss, is introduced to enforce the generator to learn the relationship between the input conditioning data and the output facies model. In addition, a progressive training approach (Karras et al., 2017) is used in GANSim, where the generator is trained progressively from shallow (coarse-resolution) to deep (fine-resolution) layers. After training with fixed input conditioning data and varying input latent vectors, the generator can produce diverse realistic facies model realizations, all conditioned to the input conditioning data. Appendix A presents more details about GANSim including the generator architecture, the condition-based loss function, and the progressive training process.

(2) CNN-based surrogate construction

In recent years, different CNN configurations for surrogate models for porous media flow have been researched depending on specific requirements, e.g., Decoder-Encoder (Wang et al., 2021), U-Net, and ConvLSTM where U-Net and LSTM are combined (Tang et al., 2021). In addition, researchers also used Cycle GANs (Zhu et al., 2017) to construct CNN-based surrogate (Sun, 2018).

When training the surrogate with a purely data-driven supervised approach, a large number of input-output labelled data pairs are required as the training data. The loss function of this approach can be formulated as

$$L_{data} = \mathbb{E}_{(m,c,d)\sim p_{(m,c,d)}} Dist(Sur(m,c),d), \tag{1}$$

where, (m,c,d) represents a combination of reservoir/rock property distributions (m), simulation related parameters (c), and the corresponding dynamic/geophysical data (d), $p_{(m,c,d)}$ is the joint distribution of (m,c,d), $Dist$ refers to a certain form of distance, and *Sur* is the CNN-based surrogate that takes as inputs the rock property distributions and simulation related parameters and outputs the corresponding dynamic/geophysical data. By minimizing L_{data}, the surrogate is trained to learn the mapping from reservoir/rock properties into dynamic/geophysical data as stored inside the training data pairs. However, with a physics-informed approach (Raissi et al., 2019), the surrogate is trained to directly learn the physical knowledge expressed by the governing PDEs. Its loss function minimizes the residual of the governing PDE and can be expressed as

$$L_{physics} = \mathbb{E}_{(m,c)\sim p_{(m,c)}} \| PDEs[Sur(m,c), m, c] \|_p, \quad (2)$$

where, $\| \cdot \|_p$ represents the L_p norm. In this equation, we take reservoir/rock property distributions (m), related parameters (c), and the dynamic/geophysical data produced from the surrogate ($Sur(m,c)$) all as inputs into the governing PDEs. In the above equation $PDEs$ symbolizes the residuals of the governing PDEs. By minimizing $L_{physics}$, the surrogate is forced to be consistent with the given PDEs.

(3) Latent vector search approaches

Among the four latent vector search algorithms explored in this work, i.e., MCMC, IES, gradient descent, and gradual deformation, the former two methods try to sample a Bayesian inferenced posterior probability distribution, while the latter two directly minimize the mismatch between the surrogate-produced and the measured dynamic/geophysical data so as to search for the optimum input latent vector each time. For the two minimization methods, multiple runs with different starting points are needed to obtain different appropriate latent vectors and different conditional facies models for approximate uncertainty analyses. Appendix B briefly describes the steps of the four search approaches in the context of GANSim-surrogate framework.

3. GANSim-surrogate framework setup for channel reservoirs

To demonstrate how GANSim-surrogate framework works and validate its effectiveness, we use it for uncertainty geomodelling of a common category of reservoir: channelized reservoir (in 2D). Here, only the conditioning of dynamic flow data is considered for illustration, although the workflow can potentially integrate conditioning of geophysical data as well.

Three types of sedimentary facies are considered in the reservoir: channel center sand, channel bank sand, and inter-channel mud. The former two facies types are lumped together as channel complex. One or multiple channel complexes may exist in one reservoir facies model, having similar features such as orientation, sinuosity, and width. This study only considers channels within $\pm$25 degrees deviation from the north-south direction. Figure 2 shows several conceptual facies model examples (obtained by object-based simulation) to illustrate the sedimentary facies types and the geological patterns of this reservoir class. Each facies model has an area of 3200m×3200m and is equally divided into 64×64 cells.

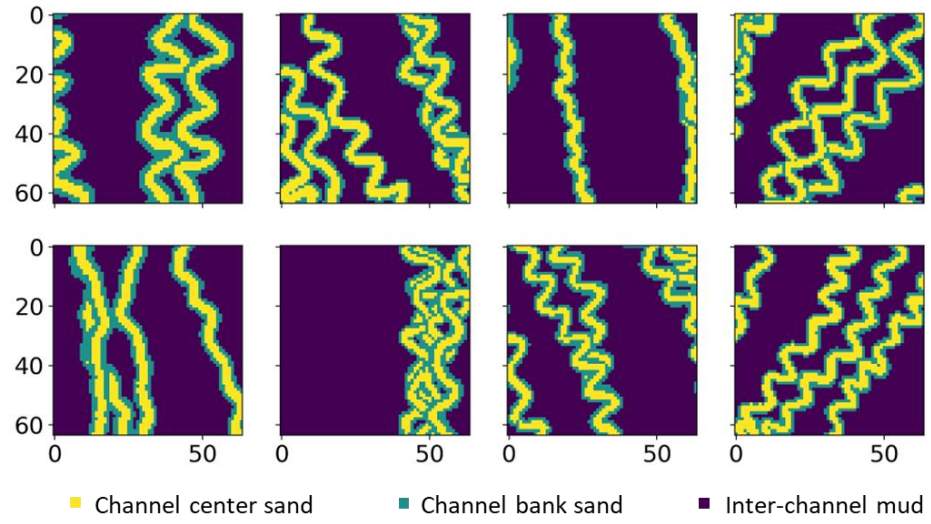

Figure 2. Conceptual channel reservoir facies model examples.

According to the GANSim-surrogate framework, in this section, we mainly focus on training a CNN-based generator producing channel reservoir facies models and a CNN-based surrogate mapping reservoir property distributions into dynamic data. Then, in section 4, the prepared GANSim-surrogate framework including the trained generator and the trained surrogate is used for conditional geomodelling and uncertainty quantification.

We simulate single-phase water flow from north to south through the channel reservoir facies model. The daily bottomhole pressure values (BHP) of different wells are regarded as the dynamic data. The surrogate uses permeability maps converted from facies models as inputs to predict the pressure distribution maps within the domain at different time steps, and finally the BHP data at different wells are obtained by sampling these pressure maps at well locations. Following section 3.1 and section 3.2 describe how the generator and the surrogate are constructed, respectively.

3.1 Construction of the generator

Song et al. (2022a) used the GANSim approach to train a generator for 2D channel reservoirs. The architecture of the generator is shown in Figure A1 (in Appendix A). The inputs include a probability map of channel complex, two indicator maps of well facies data (one for well locations and the other for facies types at well locations; see Song et al. (2021b) for detail), the facies proportion (of channel complex or mud facies type) as a type of global feature, and a latent vector consisting of 128 elements each following a standard Gaussian distribution. The training data include 35,640 conceptual facies models resulting from object-based geomodelling and the corresponding probability maps, well facies data, and facies proportion values. These conceptual facies models have the same size, resolution, sedimentary facies types, and geological patterns as in Figure 2, except that the channels are along all directions. After training, given a random group of probability map, well facies data, and facies proportion value, the generator can map them into multiple reservoir realizations which are consistent with the geological patterns of channel reservoirs and the input conditioning data.

In this study, we use the same architecture as in Song et al. (2022a). Among the 35,640 conceptual channel reservoir facies models of that study, 11,880 facies models have channel directions ranging within ± 25 degrees deviating from the north direction and are used here. The reason to limit the channel direction is to alleviate the training burden of the surrogate, which is presented in the next section. We use 11,000 facies models and the corresponding probability maps, well facies data, and channel complex proportions as the training dataset, another 440 as the development dataset for hyperparameter tunning, and the remaining 440 as the test dataset for evaluation of the results. Other settings are the same as in Song et al. (2022a), including the architecture of the discriminator, training schedule, weights for different losses, etc.

We train the generator for 10 hours with 4 GPUs (NVIDIA Tesla V100-PCIE-32GB), 20 CPUs, and 160G RAM in parallel. After training, the trained generator can map a random group of channel complex proportion value, well facies data, and probability map as well as a random latent vector into a conditional reservoir facies model realization. By changing the input latent vector, various conditional realizations can be produced. In Figure 3 (a), we randomly choose 5 facies models from the test dataset and take their corresponding probability maps, well facies data, and channel complex proportions into the trained generator to produce various facies model realizations. The channel complexes of these realizations are around the north direction, and their geological patterns are similar to that of the training facies models (see Figure 2). The input probability maps have a marked conditioning effect on these realizations. Figure 3 (b) shows the produced facies models as we gradually decrease/increase the input channel complex proportion value by 10% and 20% with other inputs fixed, indicating the influence of the input channel complex proportion on the output facies model. In addition, the reproduction accuracy of the input well facies data are 100%. The average running time for the trained generator to produce one facies model realization is about 0.0005s. From these brief evaluations, we can see that the trained generator can take the given probability map, well facies data, and channel complex proportion quickly into multiple realistic and conditional facies model realizations and thus can be used for the GANSim-surrogate framework in the next step. More complete evaluation metrics are presented in Song et al. (2021b, 2022a).

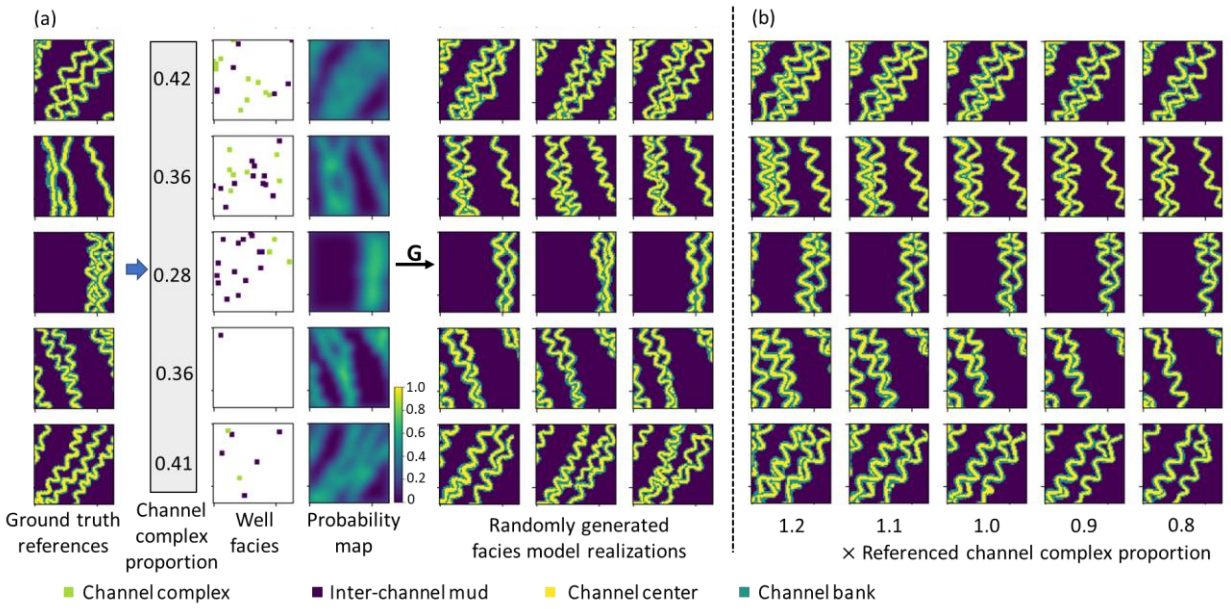

Figure 3. (a) Generated facies model realizations conditioned to the input channel complex proportion, well facies data, and channel complex probability map; (b) Generated facies model realizations with decreasing input channel complex proportion values and fixed input well facies data, probability maps, and latent vectors. G refers to the trained generator.

3.2 Construction of the flow surrogate

The surrogate aims to predict the pressure distribution map at a time step, given a channel reservoir permeability map, the boundary and initial pressure values, and the time step. Each permeability map is converted from a channel reservoir facies model by specifying a constant permeability value for each facies type: the permeability of channel center facies is specified as a value randomly sampled from 1000mD to 4000mD, the permeability of channel bank facies is calculated by multiplying the permeability of channel center of the same permeability map with a coefficient randomly sampled from 0.6 to 0.85, and the permeability of inter-channel mud is specified as a value randomly sampled from 5mD to 40mD. Different facies models correspond to different specifications of permeability values. For the flow boundary conditions, we set the east and the west boundaries of the reservoir domain as closed boundaries. The south boundary pressure is set at a constant value randomly sampled from 270bar to 330bar, and the north boundary pressure, at a constant value, is 2bar to 30bar greater than the pressure at the south boundary. The initial pressure within the domain equals the south boundary pressure. The time step ranges from 1day to 10days with an interval of 1 day. The reservoir is fully saturated with brine having a viscosity of $2cp$ and a density of $1038kg/m^3$. The compression coefficient of the reservoir including the water inside is $1.8 \times 10^{-5}\ bar^{-1}$. The water flows from north to south, and the surrogate can produce subsurface pressure maps from 1day to 10days. The dynamic BHP data at different wells can be obtained by sampling these produced pressure maps at well locations.

3.2.1 CNN architecture

The architecture of the surrogate is shown in Figure 4. The inputs include a permeability map, a boundary pressure map of which the northernmost and the southernmost rows are respectively repeated by the north and the south boundary pressure values and other cells are set to 0, an initial pressure map with the initial pressure value, and a time step map filled with the time step value. The output is a pressure map. Each input or output map of the surrogate has 64×64 cells.

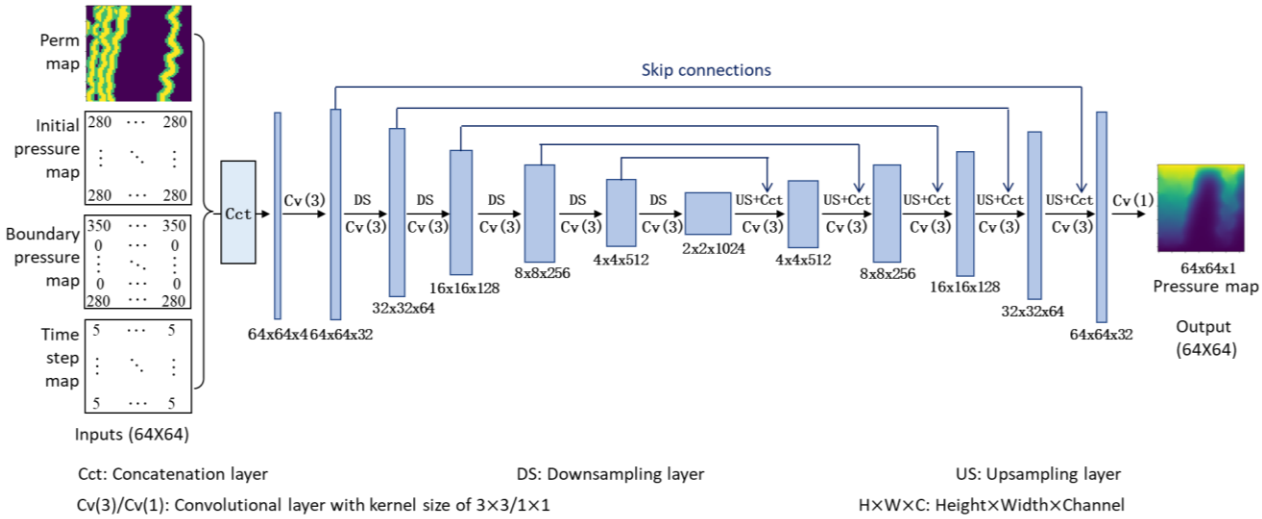

Figure 4. CNN architecture of the flow surrogate

Inside the surrogate is a U-Net CNN configuration. The four types of input maps are first concatenated and convolved to form a feature cube of 64×64×32. Then, that feature cube goes through five combined operations of downsampling and convolution to form a feature cube of 2×2×1024 containing the most abstract information of the inputs. Each downsampling operation uses an averaging method to halve the height and width of its corresponding feature cube. Next, this 2×2×1024-feature cube sequentially goes through five combined operations of upsampling, concatenation, and convolution to produce a feature cube of 64×64×32. The upsampling operations dilate the heights and widths of feature cubes by a factor of 2, using the nearest-neighbor upsampling method. Each concatenation operation combines the newly upsampled feature cube (e.g., 8×8×512-feature cube after upsamling of the 4×4×512-feature cube) with the feature cube of the same height and width produced by previous combined operations of downsampling and convolution (e.g., 8×8×256-feature cube). Finally, the 64×64×32-feature cube is converted into a pressure map of 64×64×1 as the output using a convolution operation. All convolutions have a kernel size of 3×3, except the last one for which the kernel size is 1×1. The stride length for these convolutions is 1×1. We use the leaky rectified linear unit function (LReLU) with a leaky value of 0.2 as the activation function after all convolutional layers except the last one where no activation function is applied.

Instead of the pure encoder-decoder configuration (i.e. U-Net without skip connections) used by Wang et al. (2021) to predict the pressure map, we chose to use the U-net configuration since the encoder-decoder configuration gave poor results for the channelized reservoirs with strong permeability heterogeneity.

3.2.2 Loss

Here, the surrogate is trained using a physics-informed approach. In many studies centered on physics-informed approach, a small number of input-output data pairs are also used as the training data in a semi-supervised approach to alleviate the training burden (Karniadakis et al., 2021). In this study, we only use the PDE-dominated physical law to train the surrogate, and no input-output data pair is used.

The governing equation of single-phase fluid flow in a porous reservoir media is

$$A\left[\frac{\partial\left(k(x,y)\cdot\frac{\partial p(x,y,t)}{\partial x}\right)}{\partial x}+\frac{\partial\left(k(x,y)\cdot\frac{\partial p(x,y,t)}{\partial y}\right)}{\partial y}\right]=\mu C\frac{\partial p(x,y,t)}{\partial t}, \quad (3)$$

where, x and y are coordinates along east-west and north-south directions, m; t refers to the time step in unit of days; $p(x,y,t)$ is the pressure in bars; $k(x,y)$ is the permeability in mD; μ is the viscosity of the fluid, in cp; C is the compression coefficient of the rock and the fluid inside, in bar^{-1}, and A is a unit conversion factor, 0.00852702, appropriate for these mixed units.

We use $f(k,p_N,p_S,p_I,t;\varphi)$ to denote the output pressure map of the surrogate at t day, where k is the input permeability map, p_N, p_S, and p_I denotes the north boundary, the south boundary, and the initial pressure value, and φ are the trainable parameters of the surrogate. Note that the input permeability map and the output pressure map of the surrogate each consists of 64×64 cells. We substitute the pressure term $p(x,y,t)$ in Equation (3) with $f(k,p_N,p_S,p_I,t;\varphi)$ as a map and use the finite difference method to discretize that equation as in Wang et al. (2021). The residual for each cell except the northernmost and southernmost rows at each time step is constructed as

$$R(k,p_N,p_S,p_I;\varphi)_{i,j,t}=$$
$$A\left[\frac{\left(k_{(i+1,i)/2,j}\cdot\left(f(k,p_N,p_S,p_I,t;\varphi)_{i+1,j}-f(k,p_N,p_S,p_I,t;\varphi)_{i,j}\right)\right)-\left(k_{(i,i-1)/2,j}\cdot\left(f(k,p_N,p_S,p_I,t;\varphi)_{i,j}-f(k,p_N,p_S,p_I,t;\varphi)_{i-1,j}\right)\right)}{\Delta x^2}+\right.$$
$$\left.\frac{\left(k_{i,(j+1,j)/2}\cdot\left(f(k,p_N,p_S,p_I,t;\varphi)_{i,j+1}-f(k,p_N,p_S,p_I,t;\varphi)_{i,j}\right)\right)-\left(k_{i,(j,j-1)/2}\cdot\left(f(k,p_N,p_S,p_I,t;\varphi)_{i,j}-f(k,p_N,p_S,p_I,t;\varphi)_{i,j-1}\right)\right)}{\Delta y^2}\right]-$$
$$\mu C\frac{f(k,p_N,p_S,p_I,t;\varphi)_{i,j}-f(k,p_N,p_S,p_I,t-\Delta t;\varphi)_{i,j}}{\Delta t}. \quad (4)$$

In this equation, i and j are indexes of cells along eastward and northward directions, $1\le i\le 64$, $2\le j\le 63$; $1\le t\le 10$; Δx and Δy are the length of each cell along the two directions, $\Delta x=\Delta y=50m$; Δt is the interval of the time step, i.e., $\Delta t=1$day; $k_{(i+1,i)/2,j}$ denotes the harmonic mean of permeability values at cell (i, j) and cell (i+1, j):

$$k_{(i+1,i)/2,j}=\frac{2k_{i,j}\cdot k_{i+1,j}}{k_{i,j}+k_{i+1,j}}. \quad (5)$$

The viscosity μ and the compression coefficient C are 2 cp and $1.8\times10^{-5}\ bar^{-1}$, respectively. In Equation (4), the given boundary pressure values are directly used, i.e., $f_{i,j=1,t}=p_S$, $f_{i,j=64,t}=p_N$. Since the east and west boundaries are closed boundaries, we set $f_{i=0,j,t}=f_{i=1,j,t}$ and $f_{i=65,j,t}=f_{i=64,j,t}$ in Equation (4). The initial pressure value is also directly used in the equation, i.e., $f_{i,j,t=0}=p_I$.

For each input data group (k,p_N,p_S,p_I) of the surrogate, we expect the residual term for each cell (except the northernmost and southernmost rows) to be as close to 0 as possible after training. Thus, a physics-informed loss function for each input data group (k,p_N,p_S,p_I) is formulated as

$$L(k,p_N,p_S,p_I)=\frac{1}{64\times62\times10}\sum_{1\le i\le64,2\le j\le63,1\le t\le10}\left\|R(k,p_N,p_S,p_I;\varphi)_{i,j,t}\right\|_2. \quad (6)$$

Given many such input data groups as the training data, the final loss function is

$$L = \mathbb{E}_{(k,p_N,p_S,p_I)\sim p_{(k,p_N,p_S,p_I)}} L(k, p_N, p_S, p_I), \quad (7)$$

where, $p_{(k,p_N,p_S,p_I)}$ refers to the distribution of training input data groups.

3.2.3 Training

Based on the 11,000 training, 440 development, and 440 test facies models used when constructing the generator, we build 11,000 training, 440 development, and 440 test input data groups for the surrogate. In each group, the permeability map is transformed from a facies model using the rules described in the paragraph before section 3.2.1, and the boundary and initial pressure values are randomly sampled also according to the rules described in that paragraph.

We use 4 GPUs (NVIDIA Tesla V100-PCIE-32GB), 20 CPUs, and 160G RAM to train the surrogate in parallel. The minibatch gradient descent and the Adam optimizer with default parameters (Kingma & Ba, 2014) are used. Each minibatch includes 32 training input data groups. The training is stopped after 24 hours. The loss function (Equation (7)) does not inform any constraint on the northernmost and the southernmost rows of the domain where the pressure boundary conditions are specified. Thus, the two rows of each output pressure map of the surrogate are assigned with the input north and south boundary pressure values.

3.2.4 Evaluation

We sample two input data groups, each including a permeability map and boundary and initial pressure values, from the test dataset. In the first input data group, the permeability values of the channel center, channel bank, and inter-channel mud facies are 2554mD, 1632mD, and 16mD, respectively (Figure 5), and the north boundary, south boundary, and initial pressure values are 320.6bar, 296.6bar, and 296.6bar, respectively. In the second input data group, the permeability values for the channel center, channel bank, and inter-channel mud are 1422mD, 1117mD, and 29mD, respectively (Figure 6), and the north boundary, south boundary, and initial pressure values are 319.6bar, 297.1bar, and 297.1bar, respectively. We formalize the boundary and initial pressure values and a time step (varying from 1 to 10 days) into 2D maps as shown in Figure 4. These maps as well as the permeability map are then taken as inputs into the trained surrogate to predict pressure maps after 1 to 10 days of water flow from the north to south. We also use Eclipse, a commercial software based on finite-volume PDE solutions, to compute the pressure maps for the two input data groups. Figure 5 and Figure 6 show the comparisons of the pressure maps produced by the trained surrogate and Eclipse after various days for the two cases. The absolute relative error of the surrogate-predicted results, with Eclipse results as the references, are also shown in the two figures in the form of both maps and average values.

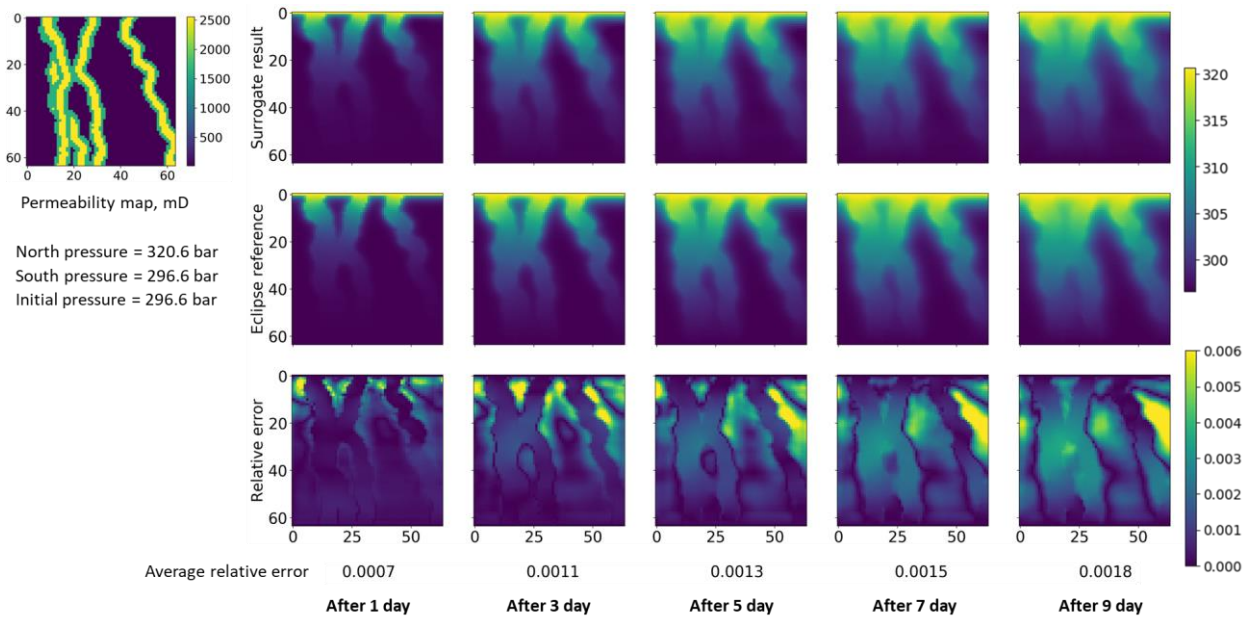

Figure 5. Comparison of pressure maps produced by the trained surrogate (the first row) and Eclipse (the second row) after various days of water flow from the north to the south. The third row shows the relative error map, with the Eclipse results as the reference. The average of absolute relative error is also calculated and given. This figure corresponds to the first input data group.

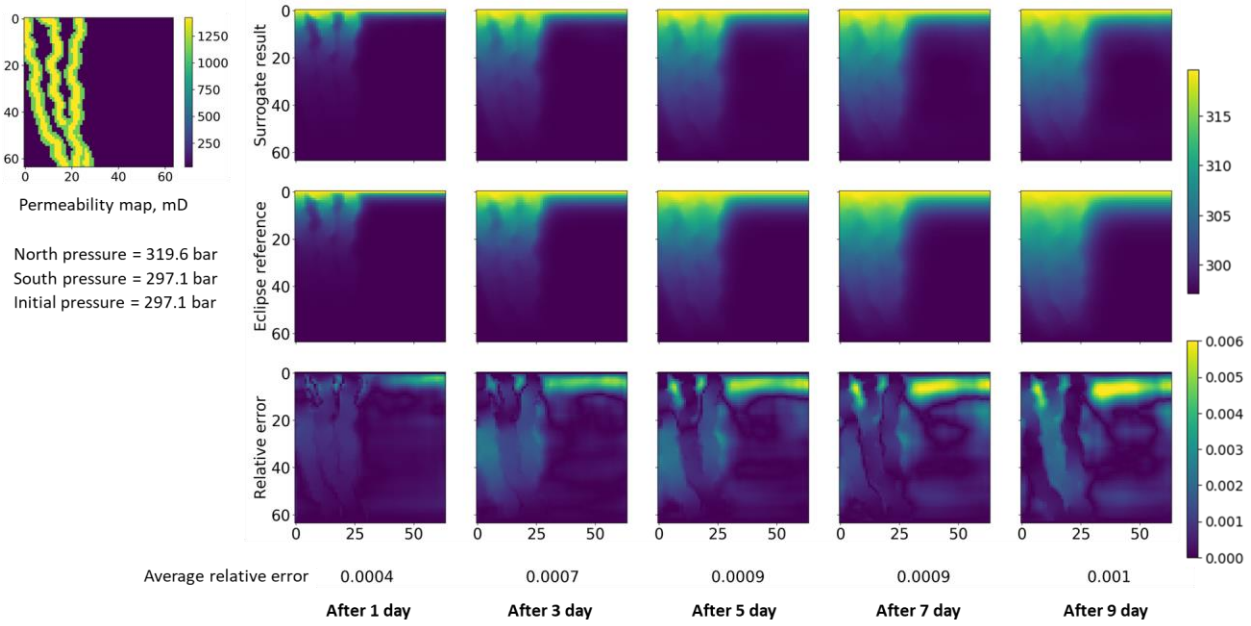

Figure 6. Comparison of pressure maps produced by the trained surrogate (the first row) and Eclipse (the second row) after various days of water flow from the north to the south. The third row shows the relative error map, with the Eclipse results as the reference. The average of absolute relative error is also calculated and given. This figure corresponds to the second input data group.

From Figure 5 and Figure 6, we can see that the surrogate-predicted pressure maps are very similar to the Eclipse-calculated references in both spatial patterns and numerical magnitude. The relative error is also quite small. Figure 7 cross-plots and compares the surrogate-predicted and the Eclipse-calculated values at 1000 points randomly sampled from the pressure maps of 1 to 10 days for the two input data groups. The least-square fit lines (red lines) of these points are very close to the one-is-to-one lines (black lines), further proving the closeness between the surrogate-predicted values and the Eclipse-calculated references.

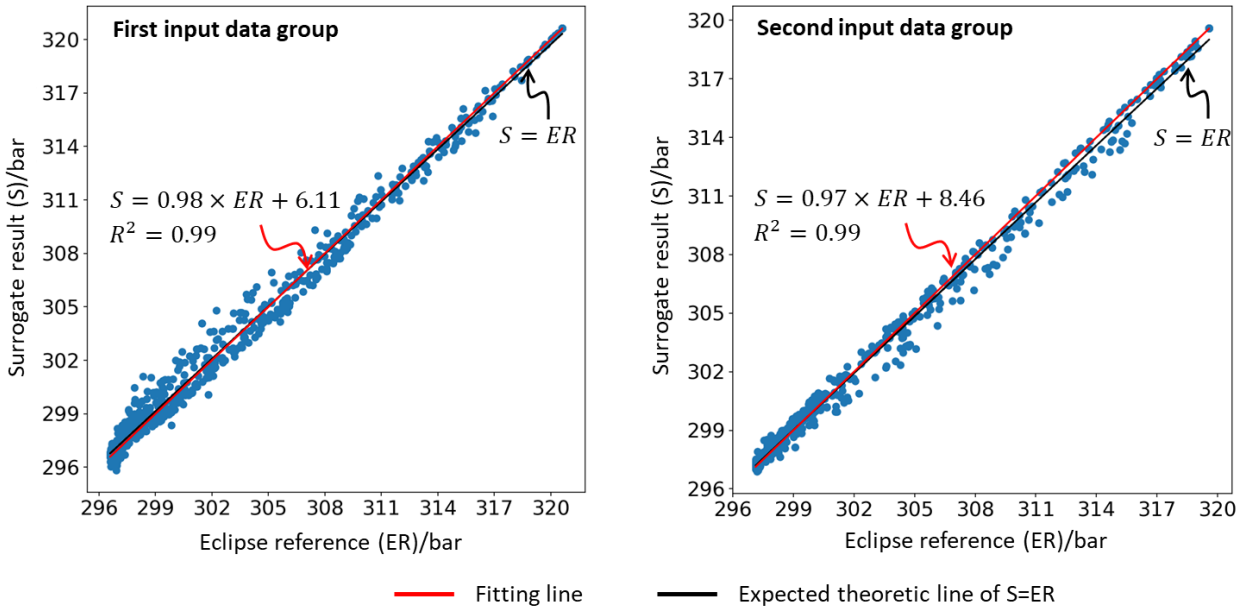

Figure 7. Cross plots between the surrogate-predicted and Eclipse-calculated pressure values at 1000 points randomly sampled from the pressure maps of 1 to 10 days for the two input data groups.

In addition, we randomly sample 100 input data groups from the test dataset and compare the surrogate-predicted pressure maps of 1 to 10 days with the Eclipse-calculated references. Figure 8 shows the histogram of the average absolute relative error for the 100 cases. We can see that the average relative error mainly ranges from 0.03% to 0.5% with a mean of 0.19%.

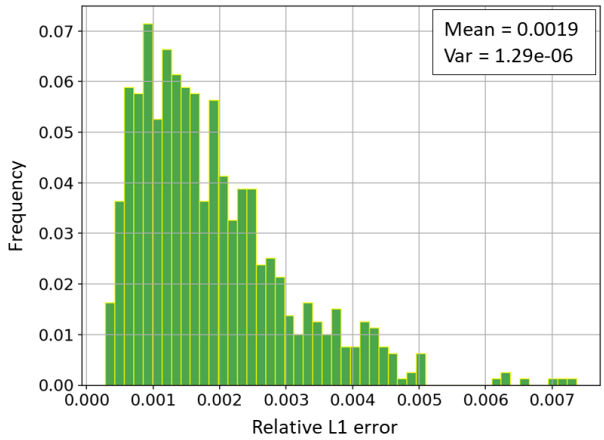

Figure 8. Histogram of the average absolute relative error for 100 random input data groups of the test dataset.

As we can see in Figure 5, Figure 6, Figure 7, and Figure 8, the accuracy of the surrogate predictions is rather high, especially given the strong heterogeneity of channel reservoirs. The surrogate takes only 0.005s to produce 10 pressure maps of 10 days for one permeability map using 1 GPU, while Eclipse uses 2.6s to simulate the same number of pressure maps using a 14 cores-based computer. The speed of the trained generator and the trained surrogate is of great significance for the success of the search of appropriate latent vectors.

4. Geomodelling of channel reservoirs with prepared GANSim-surrogate framework

In this section, first we randomly select two test channel reservoir facies models as the ground truth and obtain the four types of conditioning data (i.e., well facies data, channel complex proportion values, probability maps of channel complex, and BHP of different wells) from the two ground truth facies models. Then we use the prepared GANSim-surrogate framework, including the generator and the surrogate trained in section 3 and the four latent vector search approaches, to produce multiple posterior facies model realizations, conditioned to the above four types of conditioning data for the two test cases. Finally, the posterior realizations are evaluated, and the four latent vector search approaches are compared.

4.1 Conditioning data

(1) Test case 1

As shown in Figure 9, the ground truth facies model includes several channel complexes around the north direction. We use Gaussian kernel smoothing approach (with kernel size of 39×39 cells) to obtain the probability map of channel complex to mimic the interpretation of field geophysical data (Figure 9 (b)). Nine wells are assumed to be equally distributed in the domain, and the well facies data is obtained by sampling the facies type from the ground truth facies model at the nine well locations (Figure 9 (d)). In field cases, the channel complex proportion may be obtained by comprehensive analyses of well data, geophysical data, and geological analogy. Here, we directly calculate that proportion from the ground truth facies model (41.2%) and use it as another type of conditioning data.

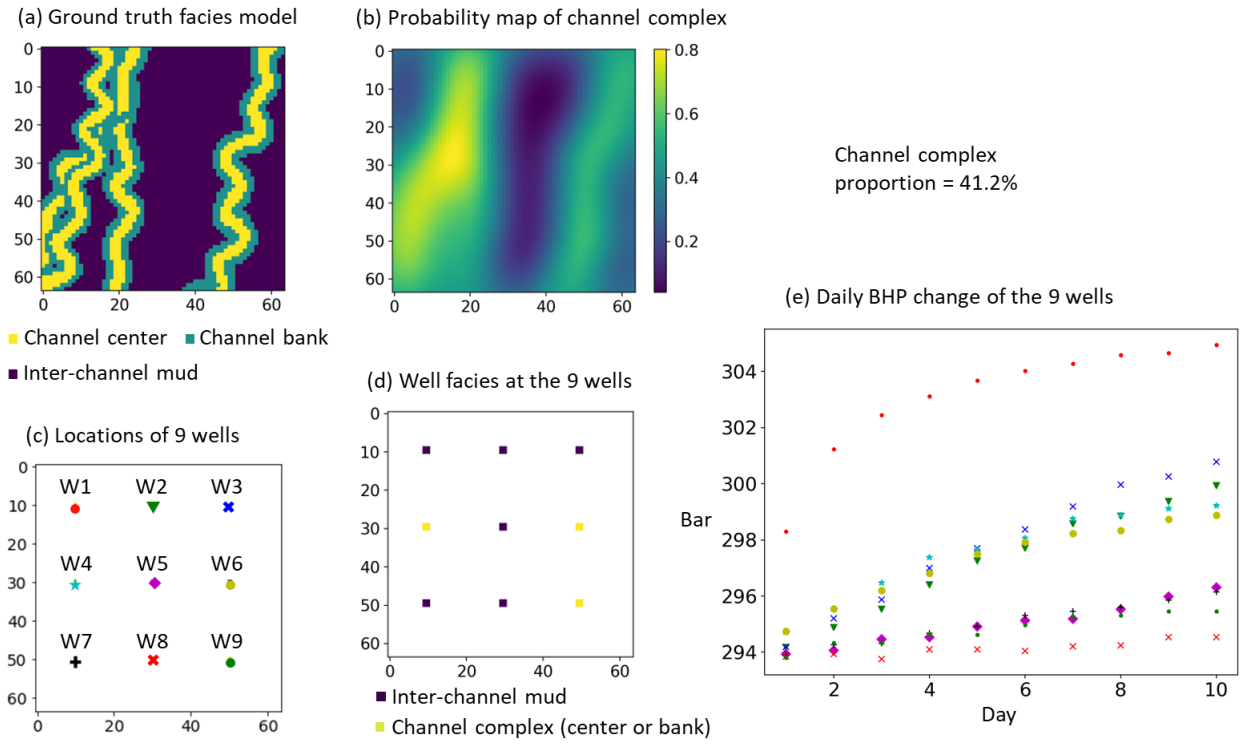

Figure 9. (a) Ground truth facies model of test case 1; (b) probability map of channel complex simulated from the ground truth facies model using Gaussian kernel smoothing; (c) locations of the nine assumed wells; (d) well facies data sampled from the ground truth facies model; (e) observed BHP data from 1 to 10 days at the nine wells; the channel complex proportion of the ground truth facies model is 41.2%.

The permeability map of the domain is obtained by setting the permeability values of the channel center, channel bank, and inter-channel mud facies as 2134mD, 1465mD, and 20mD, respectively. The constant north and south boundary pressure values of the domain are set as 308.9bar and 293.9bar, respectively. The initial pressure value of the whole domain equals to the south boundary pressure value. Based on the permeability map, we use Eclipse to simulate the pressure maps of the domain for 1 to 10 days, from which the real BHP data of the nine wells are sampled. Considering a field observation error of the field BHP data following a Gaussian distribution with the mean of 0 and standard deviation of 0.1 (i.e., $e \sim N(0,0.1)$), the observed BHP data are obtained as in Figure 9 (e).

(2) Test case 2

The selected ground truth facies model of test case 2 is shown in Figure 10 (a). Following the same procedures as in test case 1, the probability map of channel complex and the well facies data of nine equally spaced wells are obtained from the ground truth facies model (i.e., (b) and (d) of Figure 10). The channel complex proportion of the ground truth (35.5%) is used as another type of conditioning data. The permeability values of the channel center, channel bank, and inter-channel mud facies are set as 2309mD, 1405mD, and 35mD, respectively, in this case. The north boundary, the south boundary, and the initial pressure value of the domain are set as 301.5bar,

285.7bar, and 285.7bar, respectively. With the same method as in test case 1, the observed BHP data of the nine wells are obtained as in Figure 10 (e).

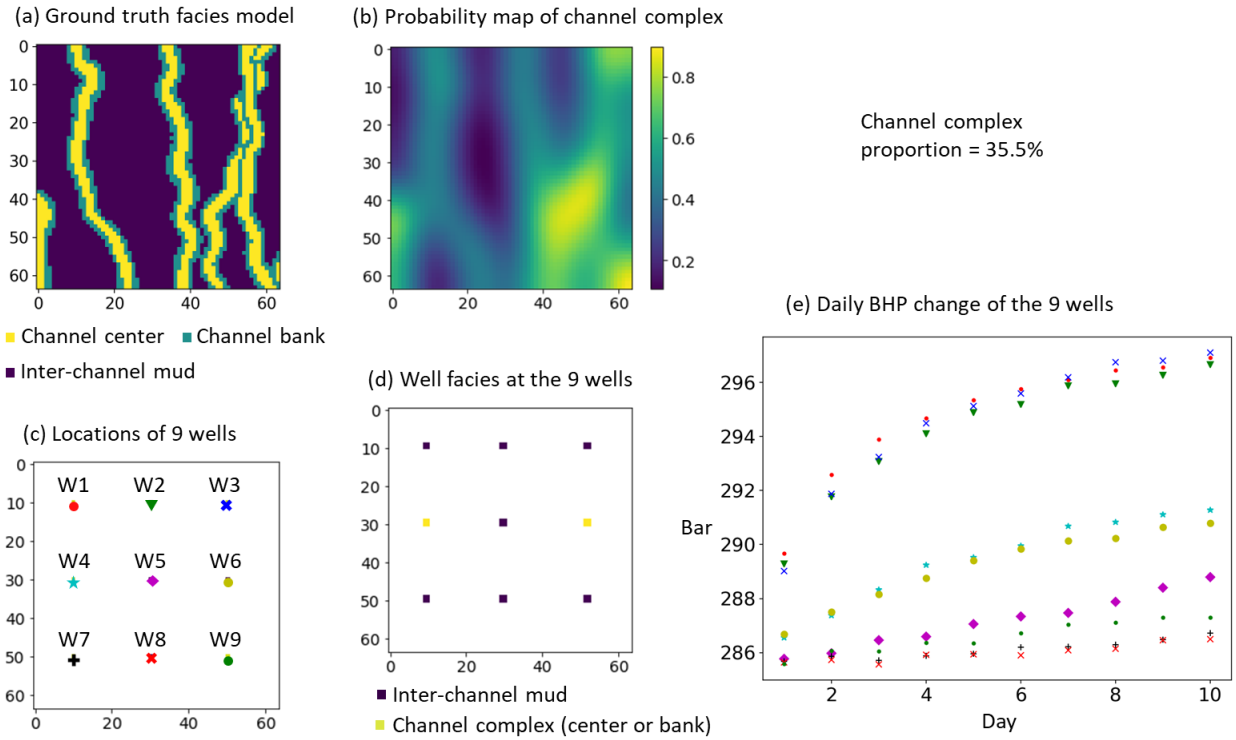

Figure 10. (a) Ground truth facies model of test case 2; (b) probability map of channel complex simulated from the ground truth facies model using Gaussian kernel smoothing; (c) locations of the nine assumed wells; (d) well facies data sampled from the ground truth facies model; (e) observed BHP data from 1 to 10 days at the nine wells; the channel complex proportion of the ground truth facies model is 35.5%.

4.2 Conditional geomodelling

Given the conditioning data of the two test cases, we follow the procedures of GANSim-surrogate framework (Figure 1) and apply the four latent vector search approaches (i.e., MCMC, IES, gradient descent, and gradual deformation) to find appropriate latent vectors, which can then be mapped into conditional facies models. In this process, each facies model produced by the generator is converted into a permeability map by assigning a constant permeability value into each facies type. We assume the permeability values for each facies to be known and hence for test case 1, we assign 2134mD, 1465mD, and 20mD into the channel center, channel bank, and inter-channel mud facies, respectively, while for test case 2, we assign 2309mD, 1405mD, and 35mD into the three facies types. Basic steps of the four latent vector search approaches are described in Appendix B and are followed here.

4.2.1 MCMC

The 128 elements of each latent vector are independent and follow a standard Gaussian distribution. As described in Appendix B.1, when proposing a new latent vector candidate z_1, each of its element (z_1^m, $m = 1,2,\dots,128$) is sampled from a proposal Gaussian distribution centered at the element of the same order of the current latent vector z_0, i.e., $z_1^m \sim N(z_0^m, 0.06)$. Each BHP data has 90 elements (i.e., ten daily BHP values for each well multiplied by nine wells). Given a random latent vector z, the likelihood of each BHP element (BHP_n, $n = 1,2,\dots,90$) is assumed to follow a Gaussian distribution: $(BHP_n|z) \sim N(g(z)_n, 0.1)$, where $g(\cdot)$ is the combined forward process of the pretrained generator, the pretrained surrogate, and the sampling of the corresponding pressure maps for BHP data at the nine well locations.

Five Markov chains, each starting from a different initial latent vector and including 20,000 inner loops, are performed for the two test cases, respectively, each taking 1258s. For each Markov chain, some initial latent vector samples during the burn-in period may not follow the posterior probability distribution and are excluded. Thus, for each sampled latent vector, we first use the trained generator and the trained surrogate to produce its BHP data BHP_{sur}, then we calculate the distance D_{BHP} between BHP_{sur} and the given observed BHP data BHP_{obs} according to

$$D_{BHP} = \frac{1}{9\times10}\sum_{n=1}^{n=9}\sum_{t=1}^{t=10}(BHP_{sur}{}_t^n - BHP_{obs}{}_t^n)^2 , \quad (8)$$

where, *n* refers to well order, and *t* refers to time step, in days. This distance is called BHP distance hereafter in this paper. Based on the BHP distance, we can clearly recognize and exclude the initial burn-in latent vectors of each Markov chain. For example, Figure 11 (a) shows the change of BHP distance (to the measured BHP data) of the initial 600 latent vector samples of one Markov chain of test case 1, in which the first 50 samples with apparently large BHP distance values are the transient samples and are excluded while the remaining ones are rather steady and should approximately follow the posterior probability distribution given the conditioning data. Finally, we obtain 69,212 and 48,587 latent vector samples in the two test cases, respectively. As is shown in Figure 11 (b) and (c), the BHP distances of these steady-state latent vectors to the measured BHP data are basically smaller than 0.35 and 0.4 in test case 1 and 2.

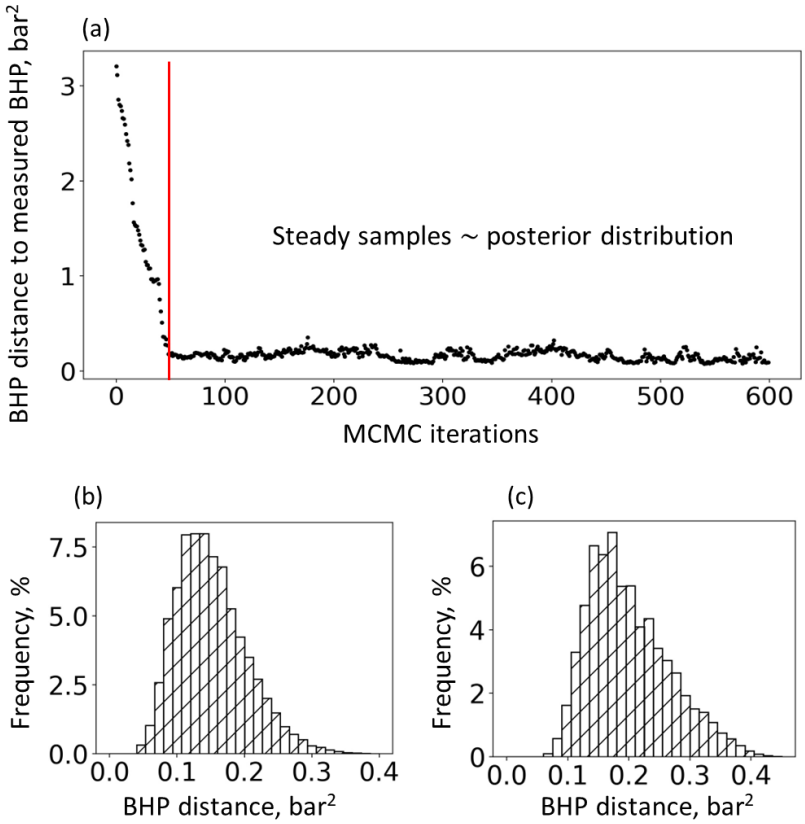

Figure 11. (a) BHP distance (to the measured BHP data) of the initial 600 latent vector samples of one Markov chain in test case 1; (b) and (c) are distributions of BHP distance (to the measured BHP data) of the steady-state latent vector samples for test case 1 and 2.

For a quick evaluation, we randomly sampled 1000 latent vectors as representatives from the sampled posterior latent vectors for both test cases, respectively. These latent vector representatives are then mapped into facies models using the trained generator and further mapped into BHP curves of the nine wells using the trained surrogate. As a benchmark for comparison, we use GANSim alone to produce 1000 random facies models that are only conditioned to the probability maps, channel complex proportions, and well facies data, but are not conditioned to the measured BHP data (i.e., purely using the trained generator to map 1000 completely random latent vectors into 1000 facies models without combining the trained surrogate and the latent vector search approaches) and map these facies models into BHP curves using the trained surrogate. The observed measured BHP data are not used in this pure GANSim process. Figure 12 and Figure 13 shows five GANSim-produced and five GANSim-surrogate (MCMC)-produced facies models for both test cases. Figure 14 and Figure 15 compares the BHP curves of the 100 GANSim-produced and 100 GANSim-surrogate (MCMC)-produced facies models for the two test cases.

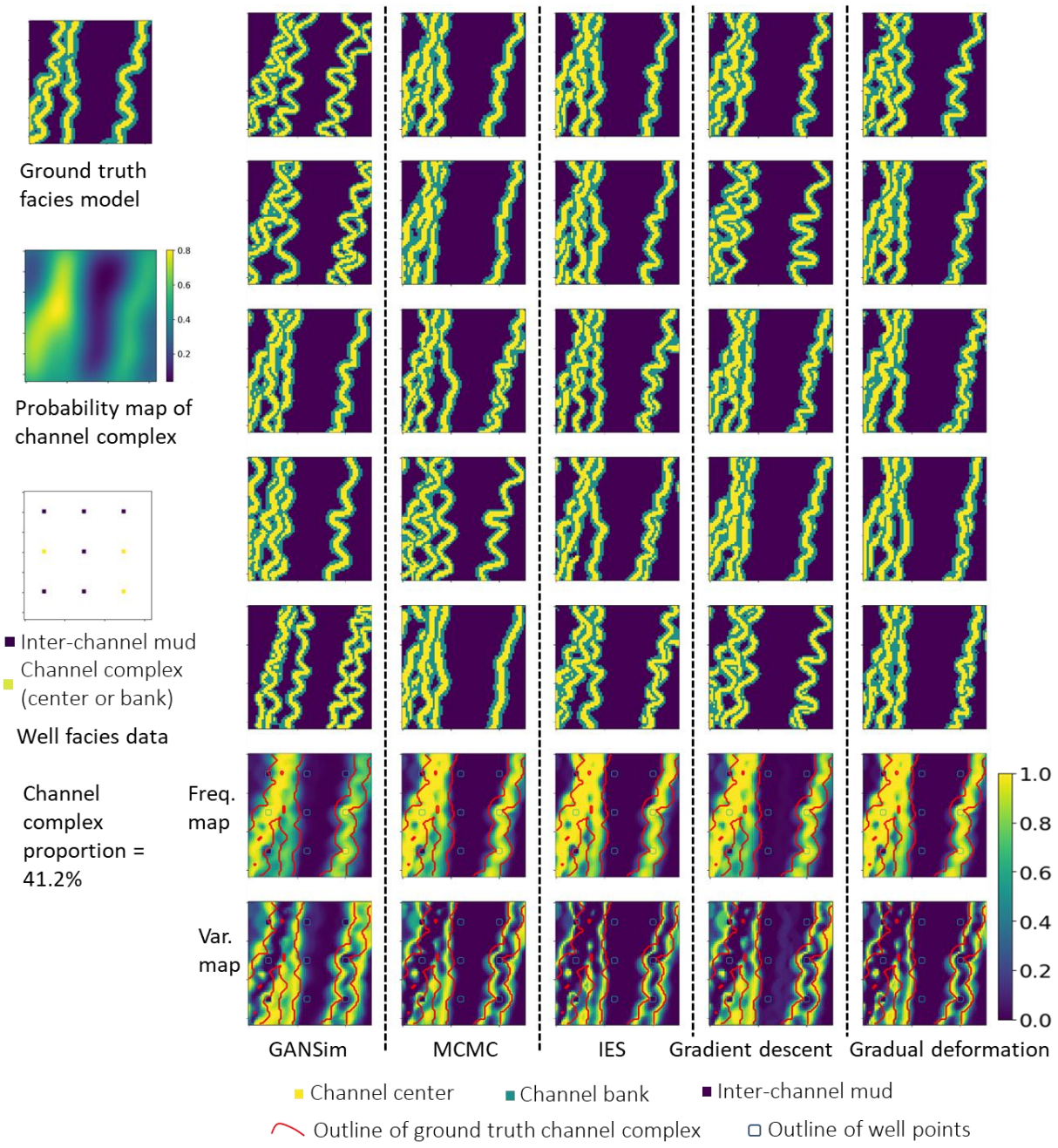

Figure 12. Random facies models produced from pure GANSim and GANSim-surrogate framework combined with four different latent vector search approaches (i.e., MCMC, IES, gradient descent, gradual deformation) in test case 1. The bottom two rows are the frequency and variance maps of channel complex calculated from 400 produced facies models.

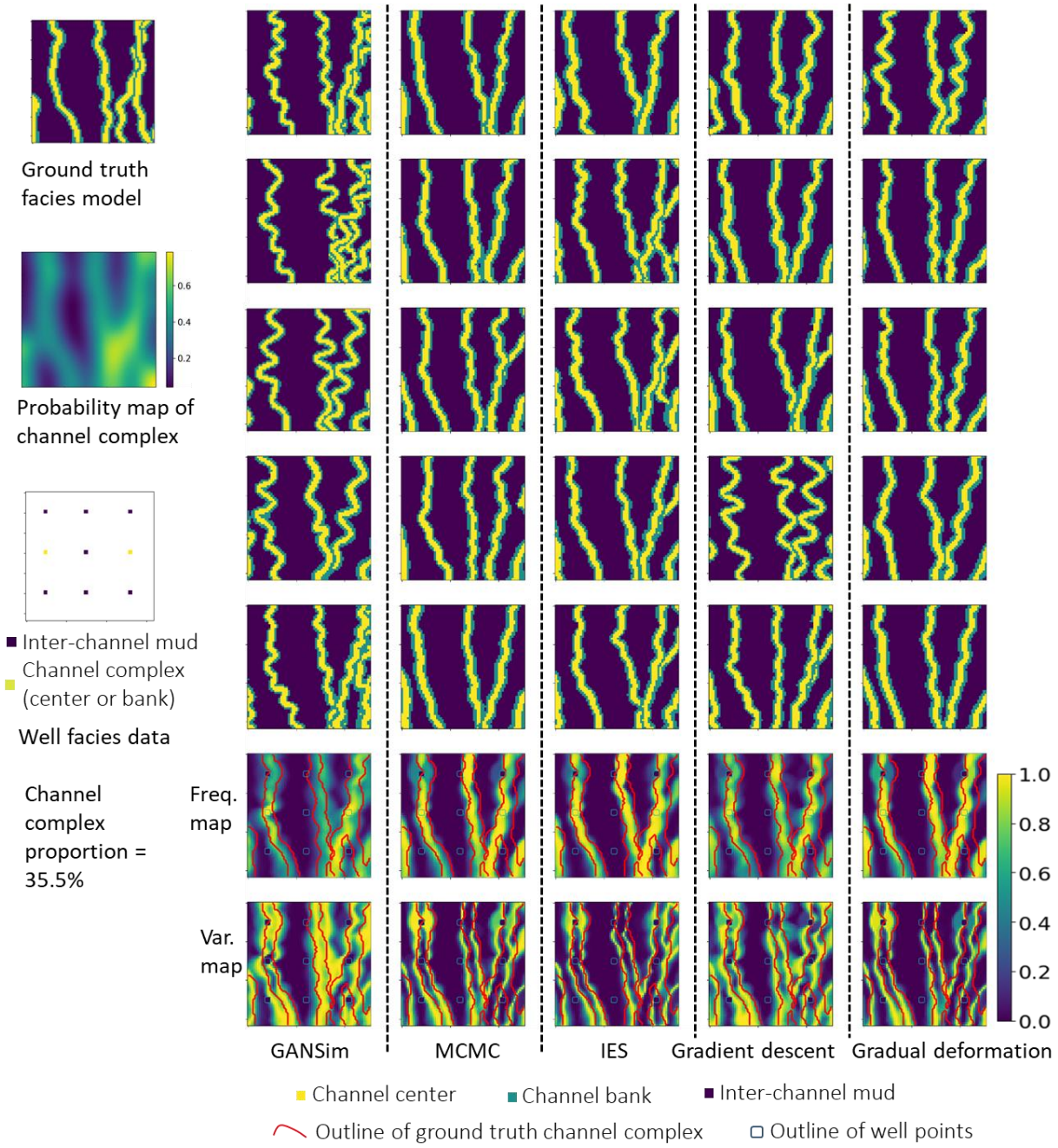

Figure 13. Random facies models produced from pure GANSim and GANSim-surrogate framework combined with four different latent vector search approaches (i.e., MCMC, IES, gradient descent, gradual deformation) in test case 2. The bottom two rows are the frequency and variance maps of channel complex calculated from 400 produced facies models.

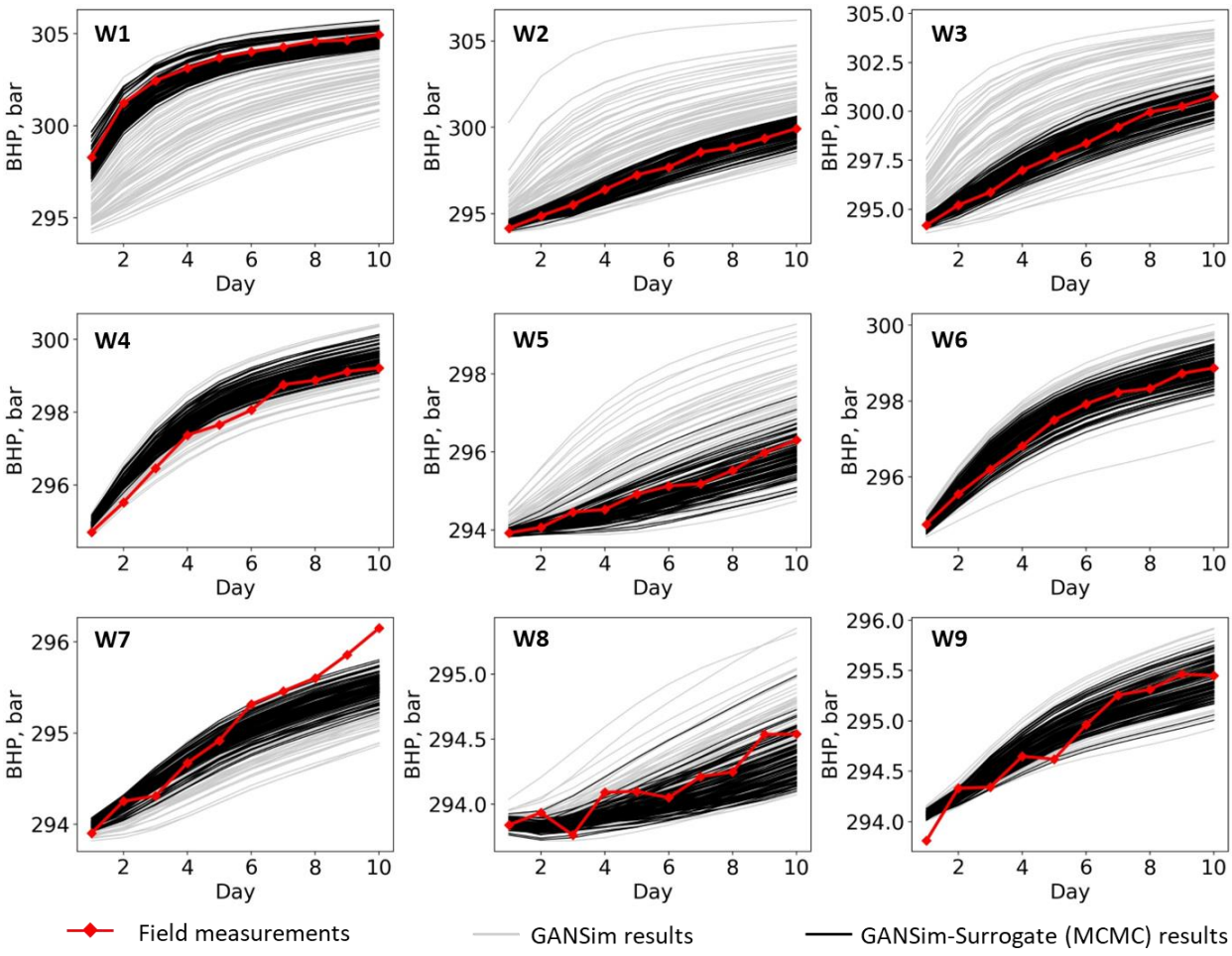

Figure 14. Comparison of the measured BHP curves and the BHP curves of facies models produced by pure GANSim (not conditioned to BHP data) and GANSim-surrogate framework with MCMC for the nine wells of test case 1.

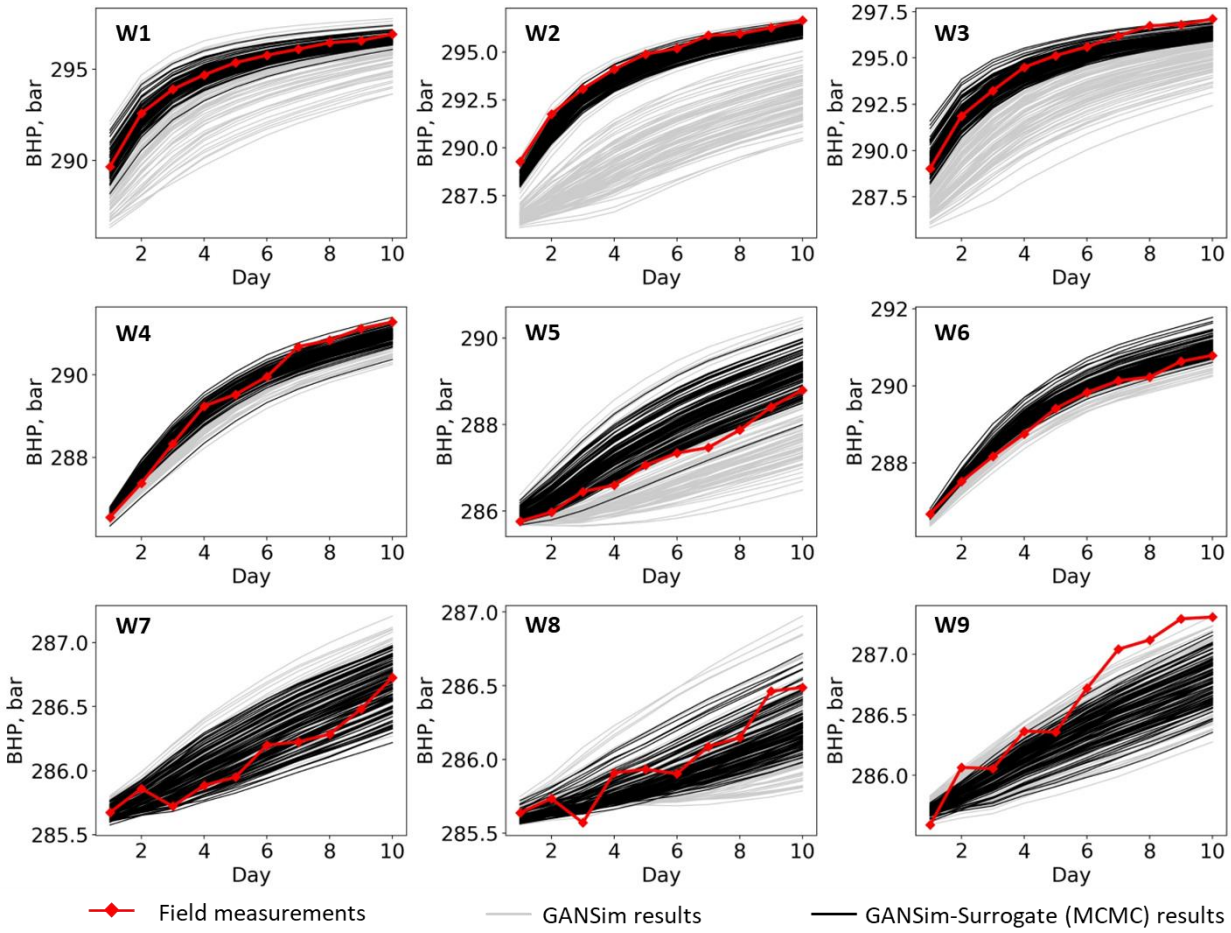

Figure 15. Comparison of measured the BHP curves and the BHP curves of facies models produced by pure GANSim and GANSim-surrogate framework with MCMC for the nine wells of test case 2. Note the different BHP-axis scales, especially for wells W7, W8 and W9, which show very little pressure variation.

4.2.2 IES

Following Appendix B.2, we set each ensemble to include 1000 latent vectors. The parameter λ_l is set as 200 constantly for all iteration steps. We perform 5 IES runs for both test cases. Each IES run is stopped once the difference of each latent vector's average BHP distance (to the measured BHP data) between two successive iteration steps becomes smaller than 0.01 (i.e., reaching convergence) or when 500 total iterations are reached. Finally, it takes 162s and 151s to get 5000 converged latent vector samples in test case 1 and 2. These latent vectors are then mapped into facies models using the trained generator. Figure 12 and Figure 13 shows five random facies models for the two test cases. Figure 16 and Figure 17 compares the BHP curves of 100 GANSim-produced and 100 GANSim-surrogate (IES)-produced facies models for the two test cases.

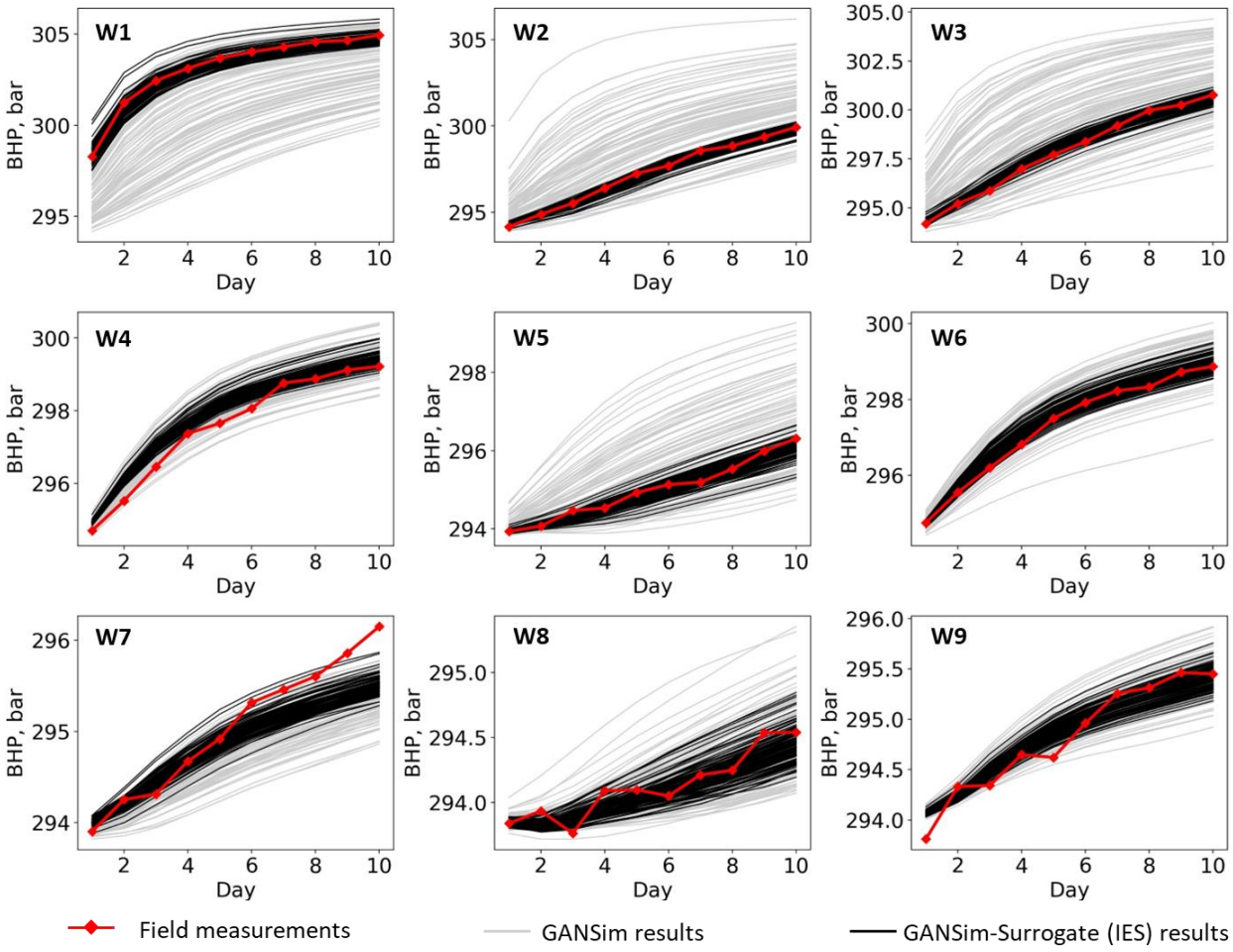

Figure 16. Comparison of the measured BHP curves and the BHP curves of facies models produced by pure GANSim and GANSim-surrogate framework with IES for the nine wells of test case 1.

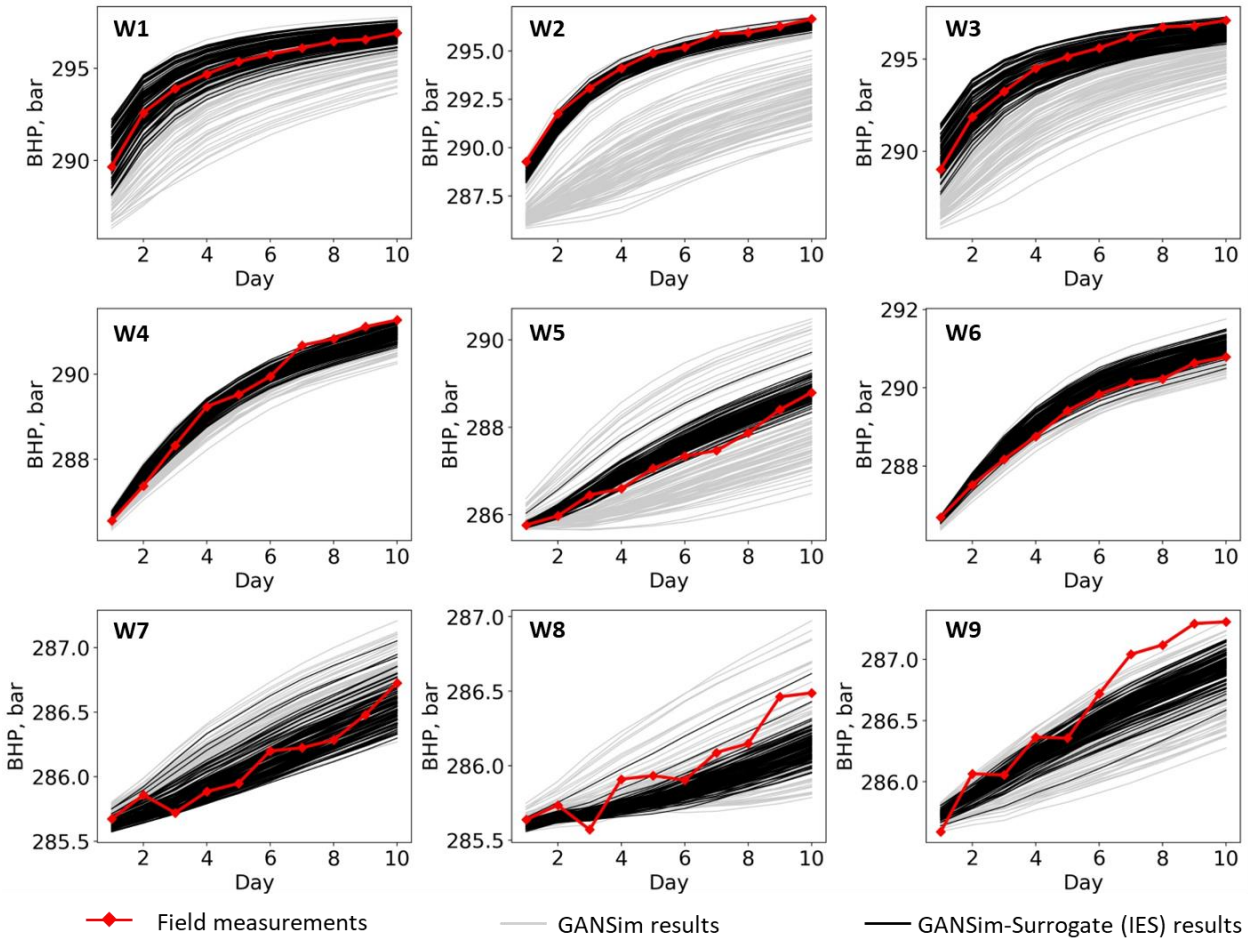

Figure 17. Comparison of the measured BHP curves and the BHP curves of facies models produced by pure GANSim and GANSim-surrogate framework with IES for the nine wells of test case 2. Note the different BHP-axis scales, especially for wells W7, W8 and W9, which show very little pressure variation.

4.2.3 Gradient descent

In gradient descent approach, for a random latent vector, we define its BHP distance to the measured BHP data as a loss. The loss is minimized with respect to the latent vector, using Adam optimizer with the default parameters (Kingma & Ba, 2014) and the learning rate of 0.01. We perform 500 rounds of gradient descent for both test cases, and in each round, each element of the initial latent vector is sampled from a standard Gaussian distribution. The gradient descent stops once the latent vector converges (i.e., the loss difference between two successive iterations becomes smaller than 0.0002) or 20000 iteration steps are reached. It takes 4619 s and 7194 s to finish the 500 rounds in test case 1 and 2, respectively. The latent vector in each round converges either to the global or to a local minimum. The BHP distances (to the measured BHP data) of the latent vectors sampled using MCMC approach are smaller than 0.35 and 0.4 in test case 1 and 2, respectively (see Figure 11 (b) and (c)). Here, we set the two values as the thresholds to distinguish local from global minima. The obtained convergent latent vectors having losses (BHP distances) larger than the thresholds are regarded as converging to local minima and

excluded. Finally, 457 and 422 latent vectors remain in test case 1 and 2. These latent vectors are then mapped into facies models, and Figure 12 and Figure 13 shows some random samples of them. Figure 18 and Figure 19 shows the BHP curves of 100 GANSim-produced and 100 GANSim-surrogate (gradient descent)-produced facies models for the two test cases.

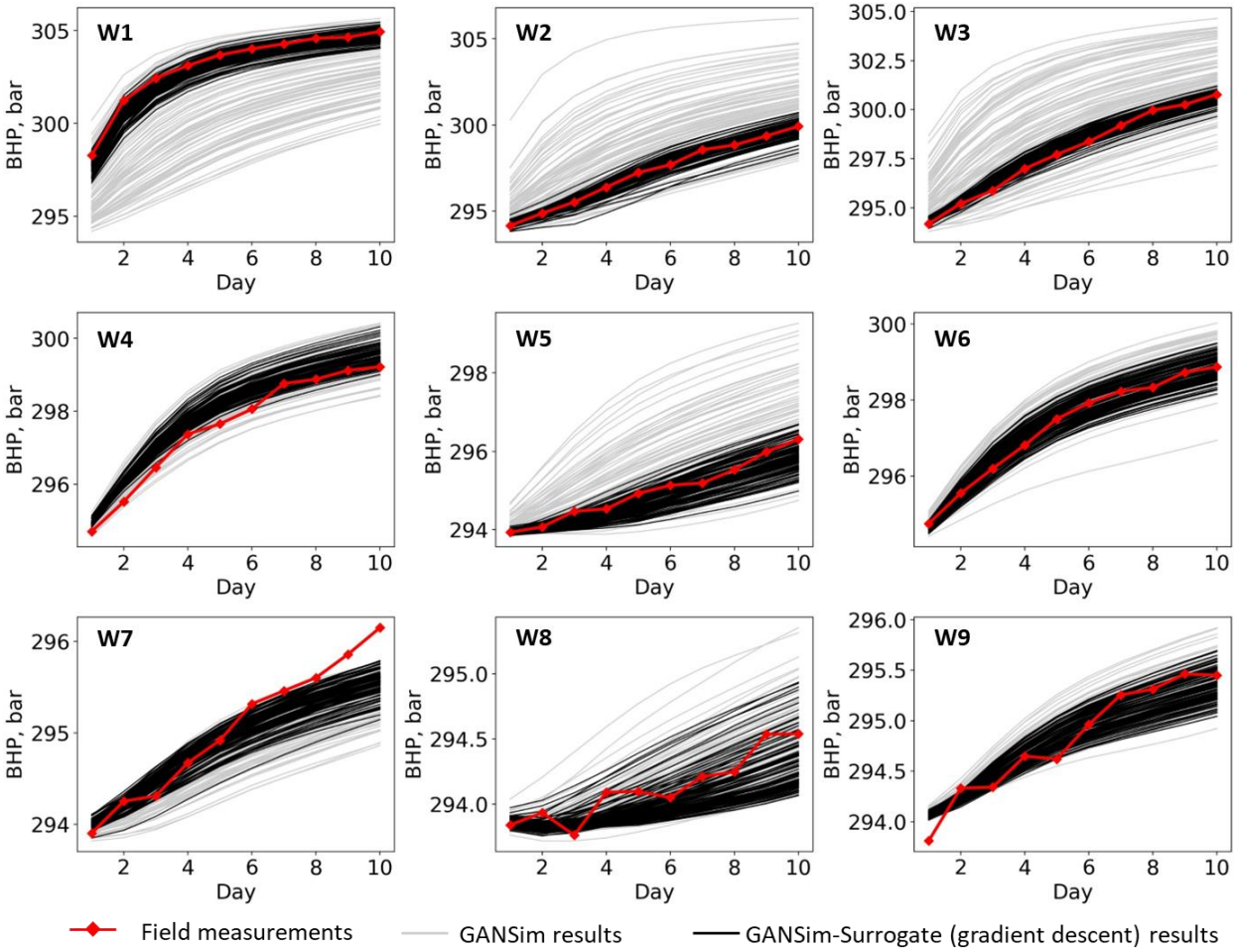

Figure 18. Comparison of the measured BHP curves and the BHP curves of facies models produced by pure GANSim and GANSim-surrogate framework with gradient descent for the nine wells of test case 1.

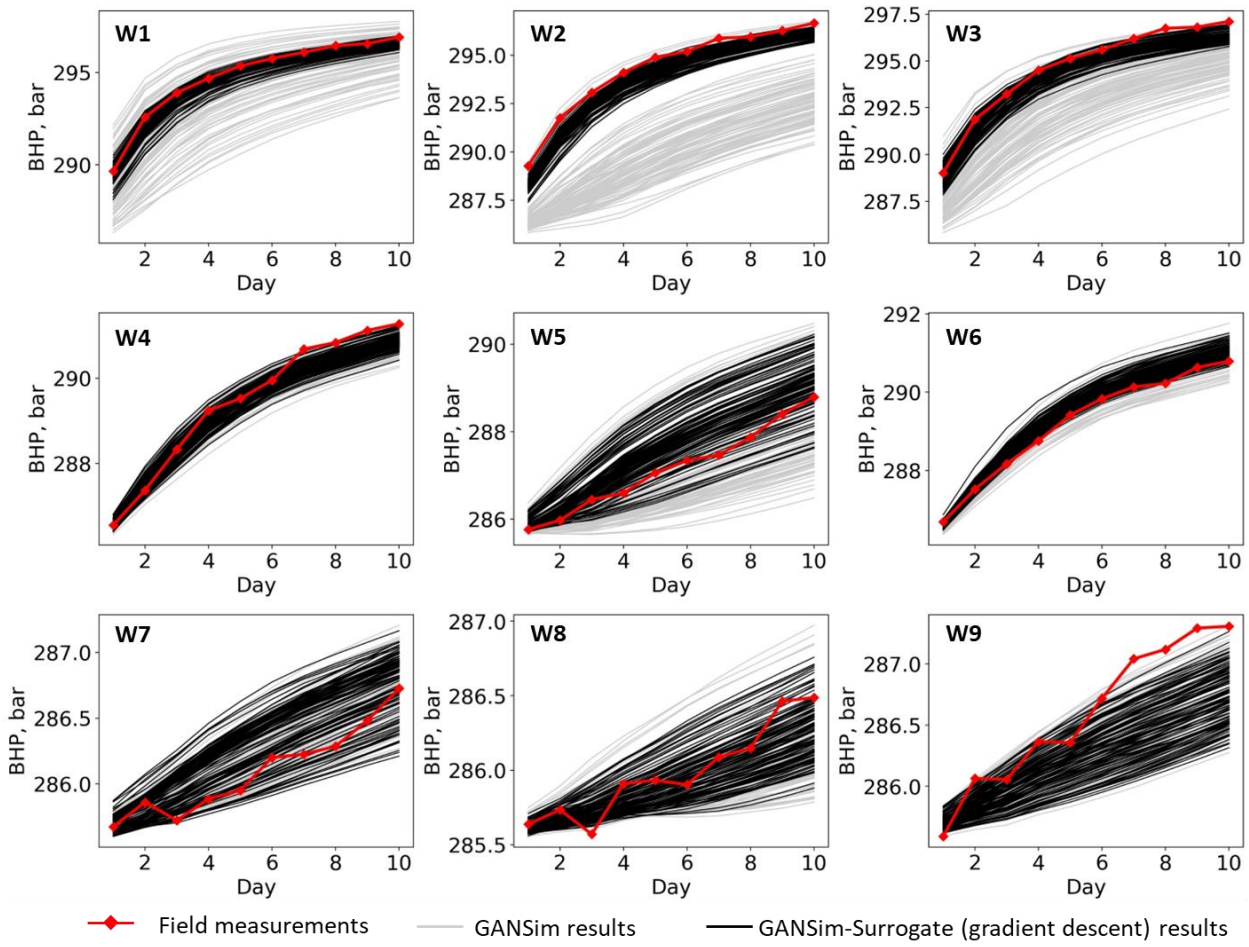

Figure 19. Comparison of the measured BHP curves and the BHP curves of facies models produced by pure GANSim and GANSim-surrogate framework with gradient descent for the nine wells of test case 2. Note the different BHP-axis scales, especially for wells W7, W8 and W9, which show very little pressure variation.

4.2.4 Gradual deformation

According to the steps described in Appendix B.4, given latent vectors z_1 and z_2, when finding the optimum r value r_{opt} from $-\pi$ to π, we first equally sample 37 r values from $-\pi$ to π (i.e., $r = -\pi,\ -35\pi/36\ , \dots , \pi$), then for each sampled r value, we calculate the corresponding latent vector ($z' = z_1 \cos r + z_2 \sin r$) and the BHP distance (to the measured BHP data; Equation (8)), and finally the r value having the minimal BHP distance is determined as r_{opt}. We perform 500 rounds of gradual deformation for each case. Each round stops once the latent vector converges (i.e., the differences of BHP distances of four successive r_{opt} all become smaller than 0.0002) or 800 inner iterations of finding r_{opt} are reached. It takes 3866 s and 4155 s to finish the 500 rounds in test case 1 and 2. Each round produces one final latent vector. The BHP distances of the 500 produced latent vectors are all smaller than 0.4 and 0.35 (the thresholds to distinguish between global and local minimum) in test case 1 and 2. These latent vectors are mapped into facies models through the trained generator, and several random ones of them are

shown in in Figure 12 and Figure 13 for the two test cases. Figure 20 and Figure 21 compares the BHP curves of 100 GANSim-produced and 100 GANSim-surrogate (gradual deformation)-produced facies models for the two test cases.

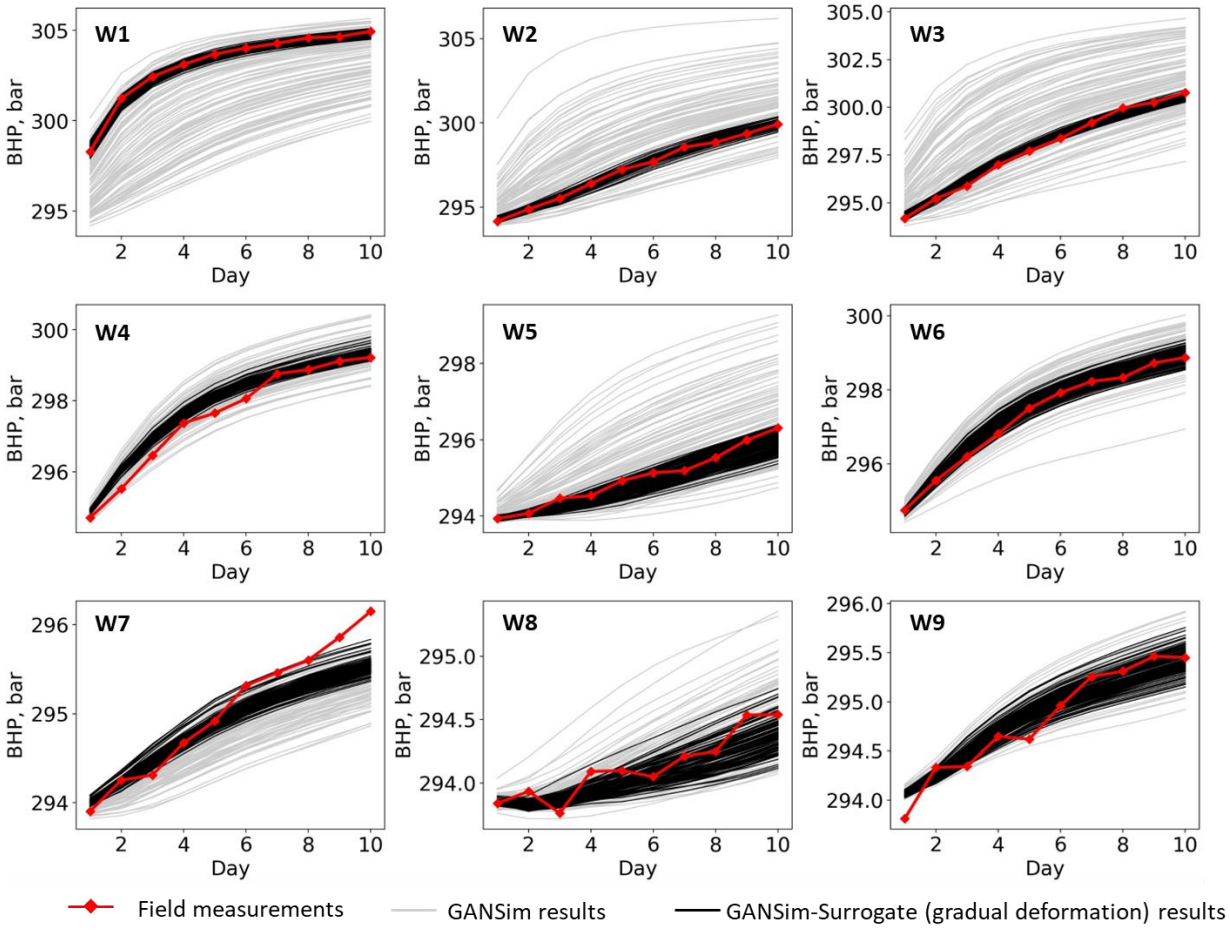

Figure 20. Comparison of the measured BHP curves and the BHP curves of facies models produced by pure GANSim and GANSim-surrogate framework with gradual deformation for the nine wells of test case 1.

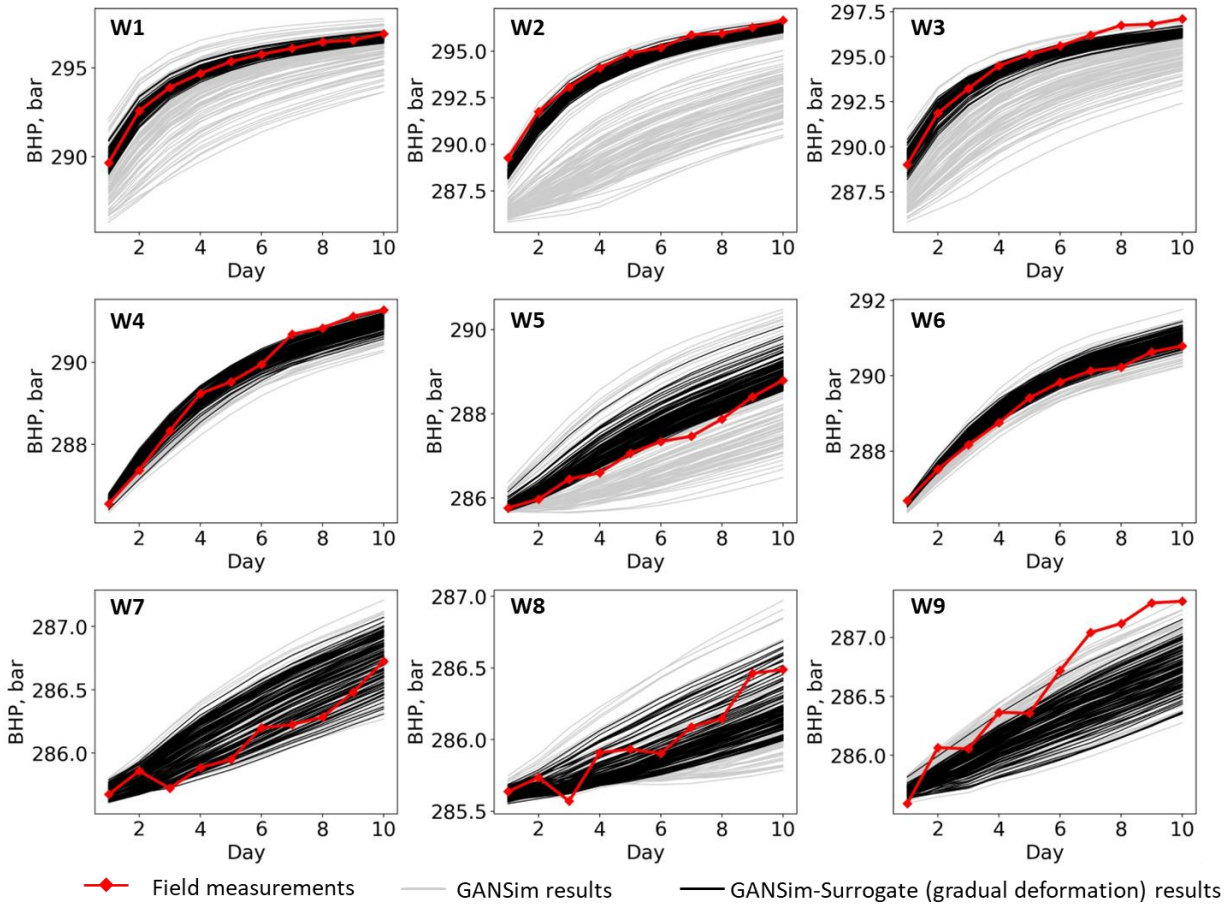

Figure 21. Comparison of the measured BHP curves and the BHP curves of facies models produced by pure GANSim and GANSim-surrogate framework with gradual deformation for the nine wells of test case 2. Note the different BHP-axis scales, especially for wells W7, W8 and W9, which show very little pressure variation.

4.3 Evaluation of conditional facies models

As we can see from Figure 12 and Figure 13, all facies models produced by the trained generator are realistic (i.e., having similar geological patterns as the training facies models in Figure 2) and diverse. The locations of the produced channel complexes in these facies models are consistent with the distribution of the high-value areas in the given probability maps. By calculation, the reproduction accuracy of the input well facies data in all produced facies models is 100% in both test cases. We calculate the channel complex proportions for the produced facies models and compare the calculated proportion values with the given conditioning one for both cases in Figure 22. It is clear that the channel complex proportions of these produced facies models are very close to the expected conditioning one in both test cases. These features of facies models (i.e., realism, variety, and conditioning to the given probability map, well facies data, and facies proportion) are inherent requirements of GANSim for the trained generator, i.e., all facies models produced by the trained GANSim generator possess these features.

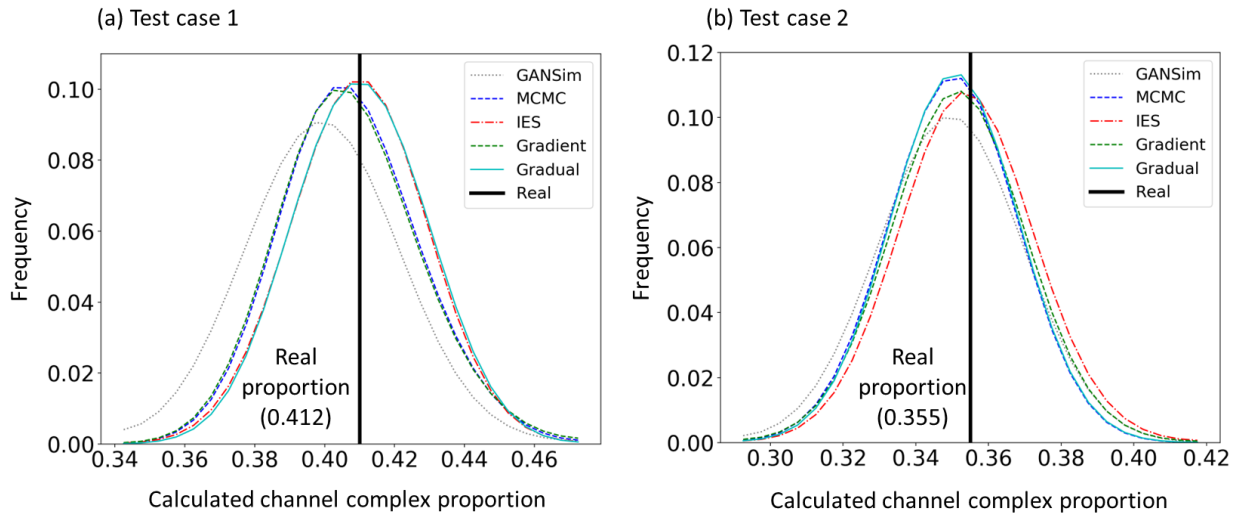

Figure 22. Probability density function curves of the channel complex proportion of the facies models resulted from GANSim and GANSim-surrogate combined with different search approaches. The vertical bold black lines represent the input conditioning channel complex proportion values.

However, as we can see from Figure 14 to Figure 21, without combining the trained surrogate, the BHP data from the GANSim-produced facies model realizations are far away from the measured BHP data. Instead, with GANSim-surrogate framework where the trained surrogate is used, no matter which latent vector search approach is combined, the final obtained facies models are all consistent with the measured BHP data (note the range differences of vertical axis among the nine subfigures of Figure 14 to Figure 21). To further validate such consistency, we randomly choose 200 facies models resulting from GANSim-surrogate framework (i.e., 50 random facies models from each search approach), use Eclipse to simulate BHP data for these 200 facies models, and compare the distributions of the BHP data produced by Eclipse and the trained surrogate. Figure 23 shows box plots of BHP distributions calculated from Eclipse and from the trained surrogate for well W1, W2, and W3 of both test cases (the measured BHP data of these three wells change most obviously over time). We can see that the BHP distributions calculated from Eclipse are very close to that calculated from the trained surrogate and close to the measured BHP data.

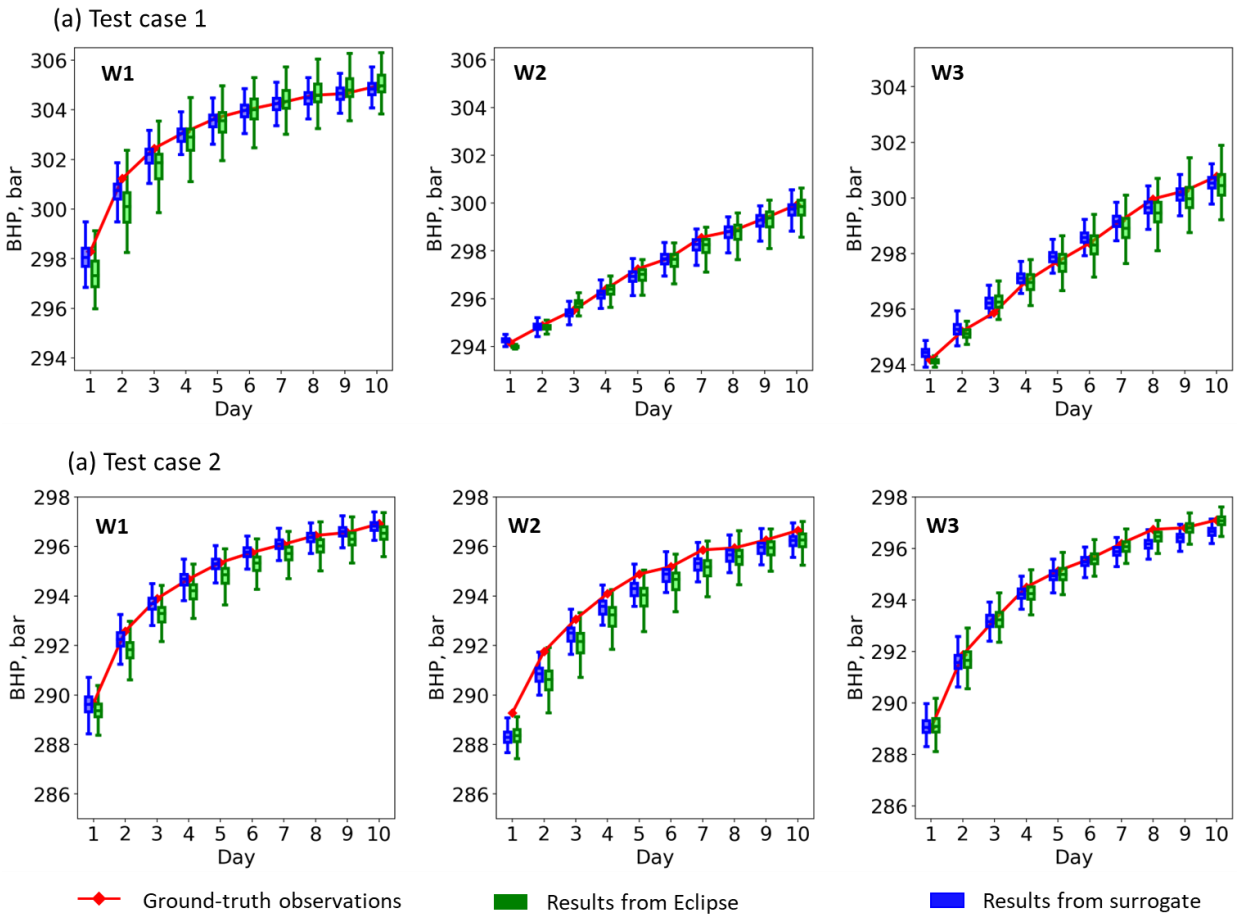

Figure 23. Box plots of BHP data at well W1, W2, and W3 calculated from 200 random posterior facies models using Eclipse and trained surrogate in both test cases. These plots have the same vertical axis range as in Figure 14 to Figure 21.

5. Discussions

5.1 Posterior distribution of conditional facies models

We use Multi-Dimensional Scaling (MDS) (Leeuw, 2005) to visually inspect the distribution change of the facies models after conditioning to the measured BHP data. First, we randomly select 100 GANSim-produced and 60 GANSim-surrogate (MCMC)-produced facies models and put them together with the ground truth facies model to form one ensemble. Then, we calculate the pairwise BHP distance between every pair of the 161 facies models of the ensemble. Next, with the calculated BHP distance as the criterion, MDS maps the ensemble of facies models into a 2D space. Since the sampling results of MCMC approximately follow the posterior probability distribution given the four types of conditioning data, here we only visualize the MCMC's results (as points), among the results of the four latent vector search approaches. The facies model distributions of other search approaches are evaluated in the next section.

As is shown in Figure 24, each point of the left scatter subplots represents one facies model, and the right density contours are calculated from the scatter plots using Gaussian kernel smoothing method. Compared to the distribution of GANSim-produced facies models which are conditioned only to probability maps, well facies data, and facies proportions, the distribution of facies models resulting from GANSim-surrogate (MCMC) where the measured BHP data are further honored, is largely shrunk towards the vicinity of the ground truth facies model. This indicates that, by further conditioning to the measured BHP data using the trained surrogate, the prediction uncertainty of the subsurface reservoir is reduced, and the prediction accuracy is increased. This can also be seen from the comparison of the frequency and variance maps of channel complexes resulting from pure GANSim and GANSim-surrogate framework in Figure 12 and Figure 13. From GANSim to GANSim-surrogate framework, the high-value areas shrink inside or closely around the ground truth channel complexes in the frequency map, and the variance map globally becomes smaller especially around the middle of the ground truth channel complexes. The distribution difference between the GANSim-produced and the GANSim-surrogate (MCMC)-produced facies models of Figure 24 represents the information value of the measured BHP data for the aim of predicting the distribution of subsurface reservoir.

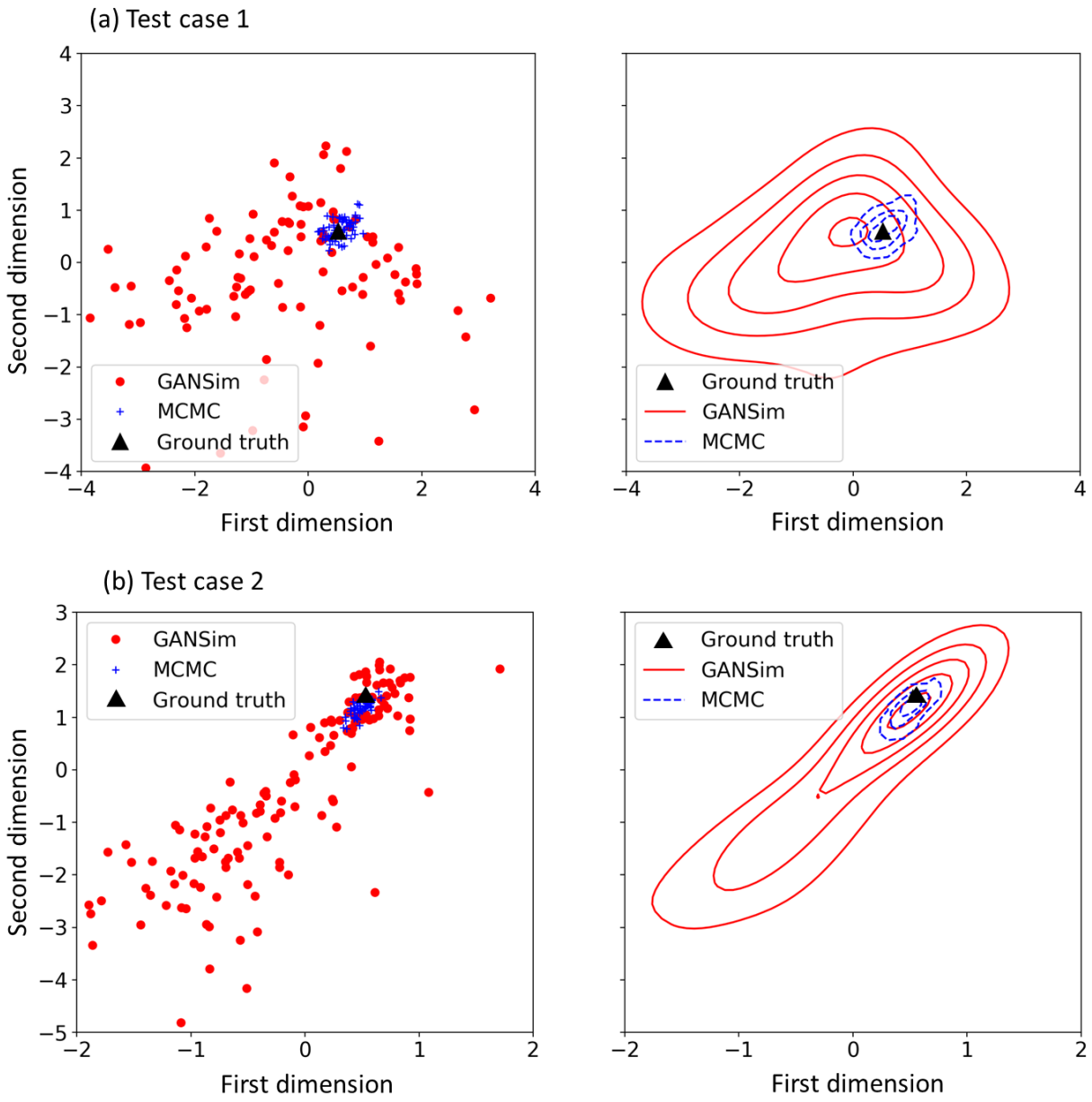

Figure 24. MDS plots of 100 GANSim-produced and 60 GANSim-surrogate (MCMC) produced facies models for both test cases. The left are the scatter plots where each point represents one 64×64-dimensional facies model. The right plots are the density contours resulting from the left scatter plots using Gaussian kernel smoothing method.

Inverse problems are non-unique and many solutions are possible that honor the conditioning data. Figure 25 shows the facies models closest to the ground truth among all the facies model results produced by different search approaches for both cases, based on the pixel-by-pixel similarity of facies type. Although these "closest" facies models are very similar to the ground truth, it is still difficult to exactly reconstruct the ground truth using the GANSim-surrogate framework. For the south-east corner of test case 2, the channel complexes of most

produced facies models are very far from the ground truth (see the produced facies models and frequency maps in Figure 13), even including some of the produced "closest" facies models (see facies models produced by MCMC and gradient descent in test case 2 of Figure 25). It is possibly because the one-to-many mapping feature of the given probability map: according to the shape of the high-value area, the south-east corner of the given probability map may correspond to either an NNW-striking channel complex consistent with the ground truth (e.g., the "closest" facies models produced by IES and gradual deformation in Figure 25) or an NNE-striking channel complex (e.g., the "closest" facies models produced by MCMC and gradient descent in Figure 25). This shows the non-uniqueness of the problem.

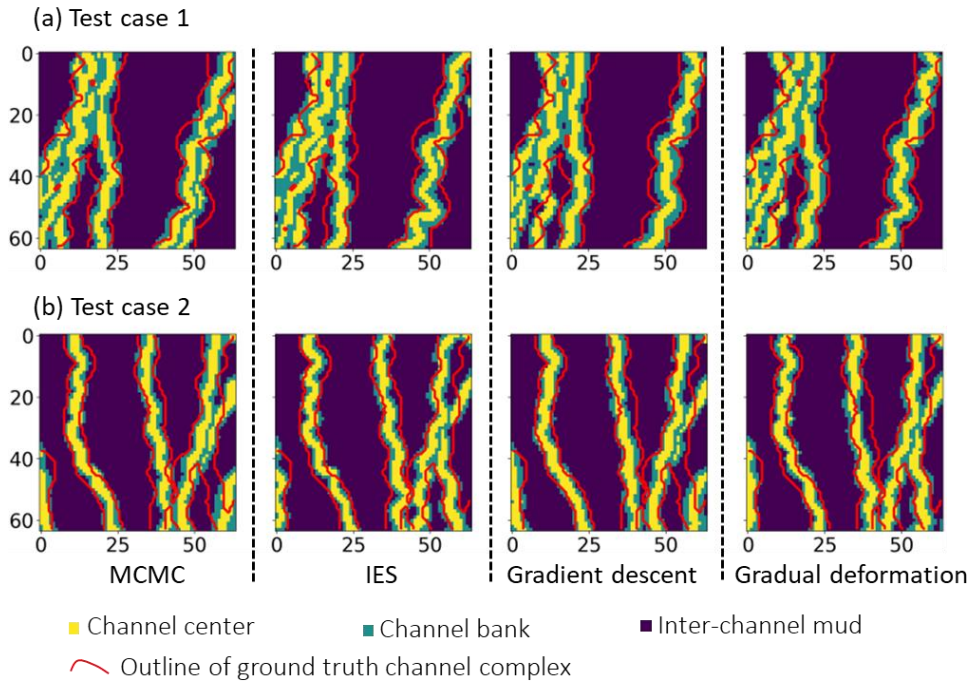

Figure 25. Facies models closest to the ground truth resulting from the GANSim-surrogate framework combined with different latent vector search approaches.

5.2 Comparison of different latent vector search approaches

In this study, all of the four latent vector search approaches produce satisfactory facies models. To compare the distribution of their results, we again use MDS with BHP distance as in Figure 24 to map into 2D space the ground truth facies model and a few random facies model realizations resulting from different search approaches (Figure 26). As the approximate representation of the posterior probability distribution given all the conditioning data, the MCMC-produced facies models (200 samples, blue crosses in Figure 26) occupy the largest 2D space (called "solution space" in this paper) among the four search approaches. The facies models of IES (200 samples), gradient descent (200 samples), and gradual deformation (160 samples, fewer than the aforementioned three search methods because the samples here are more concentrated) each only occupies a portion of the MCMC's solution space. The solution spaces

of the three search approaches are inclined to be located around the center of the MCMC's solution space (see density contour maps of Figure 26). Gradual deformation produces the smallest solution space among the four approaches.

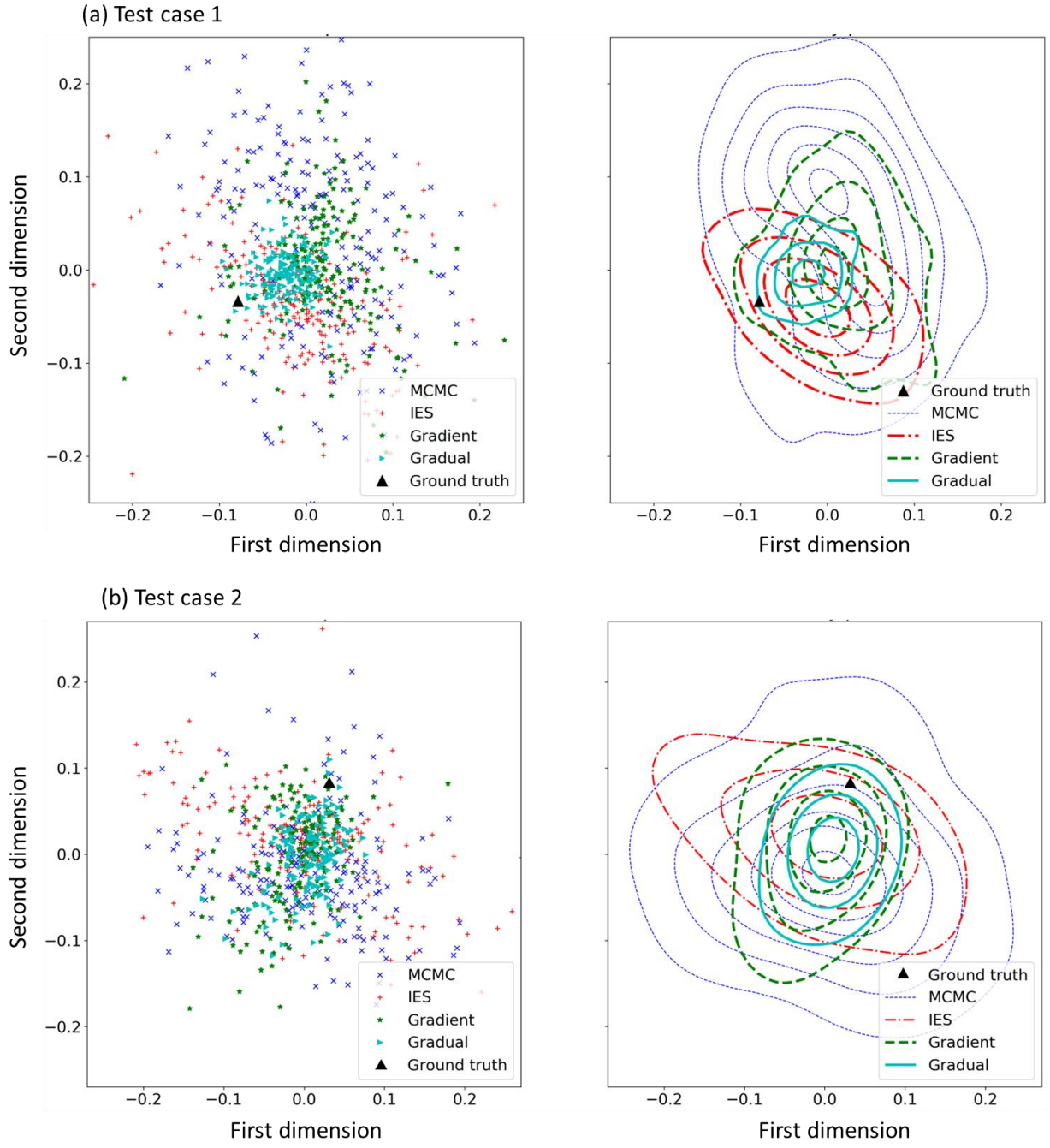

Figure 26. MDS plots of the ground truth facies model and the facies models resulting from GANSim-surrogate framework with different search approaches. The left are the scatter plots where each point represents one facies model. The right plots are the density contour maps resulting from the left scatter plots using Gaussian kernel smoothing. In the scatter plots of both

cases, 200, 200, 200 and 160 random facies models resulting from MCMC, IES, gradient descent, and gradual deformation are presented, respectively.

Table 1 compares the number of satisfactory facies models produced and the time consumed for the four search approaches for the two test cases. As optimization methods, gradient descent and gradual deformation take longer average time (about 10s) to obtain each satisfactory conditional facies model realization, compared to the two sampling methods (i.e., MCMC and IES) where each conditional facies model takes less than 0.03s on average. However, the two sampling methods do not produce conditional facies models one by one; instead, a large number of samples are concurrently produced within a relatively long time. For example, although MCMC gives samples one after another, successive resulting samples are closely related and are very similar. Therefore, if only a few conditional facies models are required, then gradient descent and gradual deformation approaches may be tried; especially if facies models with high posterior probability are required, gradual deformation may be a good option because its solution space is small and has relatively high posterior probability (see the cyan contours of Figure 26). If, on the other hand, a large number of conditional facies models are required for uncertainty evaluation, then MCMC or IES may be more efficient than the two optimization approaches.

Table 1. The number of obtained facies models and the time consumed for different latent vector search approaches for both test cases.

Searching approach	Test case 1	Test case 2
MCMC	69212fms / 1258s / 0.02s	48587fms / 1258s / 0.03s
IES	5000fms / 162s / 0.03s	5000fms / 151s / 0.03s
Gradient descent	457fms / 4619s / 10.1s	422fms / 7194s / 17.0s
Gradual deformation	500fms / 3866s / 7.7s	500fms / 4155s / 8.3s

* fms refers to facies models; the value after the second slash is the average time consumed by each satisfactory facies model.

6. Conclusions

This study proposes GANSim-surrogate framework for uncertainty quantification in geomodelling conditioned to non-spatial global features (e.g., facies proportion), sparse well facies data, low-resolution probability maps of facies (e.g., resulting from geophysical interpretation), and spatiotemporal dynamic flow data or original geophysical data. For a category of reservoirs of interest, the first step of the framework is to train i) a convolutional neural network (CNN)-based generator using the GANSim approach and ii) a CNN-based surrogate for the dynamic flow data or the geophysical data using data-driven or physics-informed neural network (PINN) approach. Then, for a new reservoir, the trained generator takes its given well facies data, global features, probability maps, and a latent vector as inputs and produces a random, realistic, and conditional facies model. Next, the produced facies model is converted into spatial distributions of rock properties (e.g., permeability, density, acoustic

velocity) that are relevant for the data simulation. Then, the trained surrogate maps the reservoir or rock property distributions into dynamic flow data or geophysical data. Finally, by minimizing the mismatch between the surrogate-produced flow or geophysical data and the actual observed ones, appropriate latent vectors are searched to give facies models that are realistic and conditioned to not only the given well facies data, global features, and probability maps but also the given dynamic flow data or geophysical data. Four latent vector search approaches are explored as options in the framework: Markov Chain Monte Karlo (MCMC), Iterative Ensemble Smoother (IES), gradient descent, and gradual deformation. The aforementioned conditioning data types are not necessarily all included in the proposed GANSim-surrogate framework.

We apply this framework for synthetic 2D channel reservoirs to validate its effectiveness. Conditioning data types include facies proportion, well facies data, probability maps, and dynamic flow data (bottomhole pressure data; BHP). The method of conditioning to geophysical data is similar to that of dynamic flow data and thus not considered in this example. A surrogate capable of flow simulation is trained using partial differential equations (PDEs) through the PINN approach. Given the above four types of conditioning data, the GANSim-surrogate framework combined with any one of the four latent vector search approaches produces realistic, diverse, and conditional facies model realizations. The average consumed time for each realization varies from 0.02s to 17s with different search approaches for two test cases. Compared to the facies models resulting from pure GANSim, which are only conditioned to the given well facies data, probability map, and facies proportion, by further conditioning to the measured BHP data, the distribution of the GANSim-surrogate-produced facies models largely shrinks towards the vicinity of the ground truth, indicating an increased prediction accuracy and a decreased uncertainty. Among the four latent vector search approaches, the facies models resulting from MCMC approximately follow the posterior distribution, while the results of other three search approaches may only occupy a portion of the complete posterior distribution. When a large number of conditional facies models are required for uncertainty evaluation, MCMC or IES are more efficient than gradient descent and gradual deformation. However, when only a few conditional facies models are required, the latter two methods may be better to try.

Acknowledgments

We acknowledge the sponsors of the Stanford Center for Earth Resources Forecasting (SCERF) and support from Prof. Steve Graham, the former Dean of the Stanford School of Earth, Energy and Environmental Sciences (now the Stanford Doerr School of Sustainability). Some of the computing for this project was performed on the Sherlock cluster at Stanford University. We would like to thank Stanford University and the Stanford Research Computing Center for providing computational resources and support that contributed to these research results.

References

Avseth, P., Mukerji, T., & Mavko, G. (2005). *Quantitative seismic interpretation: Applying rock physics tools to reduce interpretation risk*. Cambridge: Cambridge University Press. https://doi.org/10.1017/CBO9780511600074

Bosch, M., Mukerji, T., & Gonzalez, E. F. (2010). Seismic inversion for reservoir properties

combining statistical rock physics and geostatistics: A review. *Geophysics*. https://doi.org/10.1190/1.3478209

Caers, J. (2003a). Efficient gradual deformation using a streamline-based proxy method. *Journal of Petroleum Science and Engineering*. https://doi.org/10.1016/S0920-4105(03)00040-8

Caers, J. (2003b). History matching under training-image-based geological model constraints. *SPE Journal*, *8*(03), 218–226. https://doi.org/10.2118/74716-PA

Caers, J., & Hoffman, T. (2006). The probability perturbation method: A new look at Bayesian inverse modeling. *Mathematical Geology*, *38*(1), 81–100. https://doi.org/10.1007/s11004-005-9005-9

Chan, S., & Elsheikh, A. H. (2017). Parametrization and generation of geological models with generative adversarial networks. *ArXiv Preprint*, arXiv: 1708.01810.

Chan, S., & Elsheikh, A. H. (2019). Parametric generation of conditional geological realizations using generative neural networks. *Computational Geosciences*, *23*(5), 925–952. https://doi.org/10.1007/s10596-019-09850-7

Chang, H., Liao, Q., & Zhang, D. (2017). Surrogate model based iterative ensemble smoother for subsurface flow data assimilation. *Advances in Water Resources*. https://doi.org/10.1016/j.advwatres.2016.12.001

Chen, Y., & Oliver, D. S. (2013). Levenberg-Marquardt forms of the iterative ensemble smoother for efficient history matching and uncertainty quantification. *Computational Geosciences*. https://doi.org/10.1007/s10596-013-9351-5

Deutsch, C. V. (2002). *Geoestatistical reservoir modeling*. Oxford: Oxford University Press.

Dupont, E., Zhang, T., Tilke, P., Liang, L., & Bailey, W. (2018). Generating realistic geology conditioned on physical measurements with Generative Adversarial Networks. In *Stat* (pp. 8–16).

Efendiev, Y., Jin, B., Michael, P., & Tan, X. (2015). Multilevel markov chain monte carlo method for high-contrast single-phase flow problems. *Communications in Computational Physics*, *17*(1), 259–286. https://doi.org/10.4208/cicp.021013.260614a

Goodfellow, I., Pouget-Abadie, J., Mirza, M., Xu, B., Warde-Farley, D., Ozair, S., et al. (2014). Generative Adversarial Networks. In *Advances in Neural Information Processing Systems 27* (pp. 10–23). https://doi.org/10.1001/jamainternmed.2016.8245

Hu, L. Y. (2000). Gradual deformation and iterative calibration of Gaussian-related stochastic models. *Mathematical Geology*. https://doi.org/10.1023/A:1007506918588

Hu, L. Y. (2008). Extended probability perturbation method for calibrating stochastic reservoir models. *Mathematical Geosciences*, *40*, 875–885. https://doi.org/10.1007/s11004-008-9158-4

Hu, L. Y., Blanc, G., & Noetinger, B. (2001). Gradual deformation and iterative calibration of sequential stochastic simulations. *Mathematical Geology*. https://doi.org/10.1023/a:1011088913233

Jafarpour, B., & Khodabakhshi, M. (2011). A probability conditioning method (PCM) for nonlinear flow data integration into multipoint statistical facies simulation. *Mathematical*

Geosciences, *43*, 133–164. https://doi.org/10.1007/s11004-011-9316-y

Karniadakis, G. E., Kevrekidis, I. G., Lu, L., Perdikaris, P., Wang, S., & Yang, L. (2021). Physics-informed machine learning. *Nature Reviews Physics*. https://doi.org/10.1038/s42254-021-00314-5

Karras, T., Aila, T., Laine, S., & Lehtinen, J. (2017). Progressive growing of GANs for improved quality, stability, and variation. *ArXiv Preprint*, arXiv: 1710.10196.

Kingma, D., & Ba, J. (2014). Adam: a method for stochastic optimization. *ArXiv Preprint*, arXiv:1412.6980. https://doi.org/10.1109/ICCE.2017.7889386

Laloy, E., Hérault, R., Jacques, D., & Linde, N. (2018). Training-image based geostatistical inversion using a spatial Generative Adversarial Neural Network. *Water Resources Research*, *54*(1), 381–406. https://doi.org/10.1002/2017WR022148

Laloy, E., Linde, N., Ruffino, C., Hérault, R., Gasso, G., & Jacques, D. (2019). Gradient-based deterministic inversion of geophysical data with generative adversarial networks: Is it feasible? *Computers and Geosciences*. https://doi.org/10.1016/j.cageo.2019.104333

Leeuw, J. de. (2005). Modern Multidimensional Scaling: Theory and Applications (Second Edition). *Journal of Statistical Software*. https://doi.org/10.18637/jss.v014.b04

Li, H., & Zhang, D. (2009). Efficient and accurate quantification of uncertainty for multiphase flow with the probabilistic collocation method. *SPE Journal*. https://doi.org/10.2118/114802-PA

Liao, Q., Zeng, L., Chang, H., & Zhang, D. (2019). Efficient history matching using the markov-chain monte carlo method by means of the transformed adaptive stochastic collocation method. *SPE Journal*, *24*(4), 1468–1489. https://doi.org/10.2118/194488-PA

Ma, X., AlHarbi, M., Dalta-Gupta, A., & Efendiev, Y. (2008). An efficient two-stage sampling method for uncertainty quantification in history matching geological models. *SPE Journal*, *13*(1), 77–87. https://doi.org/10.2118/102476-PA

Mariethoz, G., & Caers, J. (2014). *Multiple-point geostatistics: stochastic modeling with training images*. New York: John Wiley & Sons. https://doi.org/10.1002/9781118662953

Mo, S., Zabaras, N., Shi, X., & Wu, J. (2020). Integration of Adversarial Autoencoders With Residual Dense Convolutional Networks for Estimation of Non-Gaussian Hydraulic Conductivities. *Water Resources Research*. https://doi.org/10.1029/2019WR026082

Mosser, L., Dubrule, O., & Blunt, M. J. (2020). Stochastic seismic waveform inversion using Generative Adversarial Networks as a geological prior. *Mathematical Geosciences*, *52*(1), 53–79. https://doi.org/10.1007/s11004-019-09832-6

Nesvold, E., & Mukerji, T. (2021). Simulation of fluvial patterns with GANs trained on a data set of satellite imagery. *Water Resources Research*, *57*(22). https://doi.org/10.1029/2019WR025787.

Raissi, M., Perdikaris, P., & Karniadakis, G. E. (2019). Physics-informed neural networks: A deep learning framework for solving forward and inverse problems involving nonlinear partial differential equations. *Journal of Computational Physics*, *378*, 686–707.

Song, S., Mukerji, T., & Hou, J. (2021a). GANSim: Conditional facies simulation using an

improved progressive growing of Generative Adversarial Networks (GANs). *Mathematical Geosciences*. https://doi.org/https://doi.org/10.1007/s11004-021-09934-0

Song, S., Mukerji, T., & Hou, J. (2021b). Geological facies modeling based on progressive growing of Generative Adversarial Networks (GANs). *Computational Geosciences*. https://doi.org/https://doi.org/10.1007/s10596-021-10059-w

Song, S., Mukerji, T., & Hou, J. (2022). Bridging the gap between geophysics and geology with Generative Adversarial Networks (GANs). *IEEE Transactions on Geoscience and Remote Sensing*, *60*, 1–11. https://doi.org/10.1109/TGRS.2021.3066975

Song, S., Mukerji, T., Hou, J., Zhang, D., & Lyu, X. (2022). GANSim-3D for conditional geomodelling: theory and field application. *Water Resources Research, 58. https://doi.org/10.1029/2021WR031865*

Sun, A. Y. (2018). Discovering State-Parameter Mappings in Subsurface Models Using Generative Adversarial Networks. *Geophysical Research Letters*. https://doi.org/10.1029/2018GL080404

Tang, M., Liu, Y., & Durlofsky, L. J. (2021). Deep-learning-based surrogate flow modeling and geological parameterization for data assimilation in 3D subsurface flow. *Computer Methods in Applied Mechanics and Engineering*. https://doi.org/10.1016/j.cma.2020.113636

Wang, N., Chang, H., & Zhang, D. (2021). Theory-guided Auto-Encoder for surrogate construction and inverse modeling. *Computer Methods in Applied Mechanics and Engineering*. https://doi.org/10.1016/j.cma.2021.114037

Wu, J., Zhang, C., Xue, T., Freeman, W. T., & Tenenbaum, J. B. (2016). Learning a probabilistic latent space of object shapes via 3D Generative-Adversarial modeling. In *In Proceedings of the 30th International Conference on Neural Information Processing Systems* (pp. 82–90).

Xu, R., Zhang, D., & Wang, N. (2022). Uncertainty quantification and inverse modeling for subsurface flow in 3D heterogeneous formations using a theory-guided convolutional encoder-decoder network. *Journal of Hydrology, In press*.

Zhang, T. F., Tilke, P., Dupont, E., Zhu, L. C., Liang, L., & Bailey, W. (2019). Generating geologically realistic 3D reservoir facies models using deep learning of sedimentary architecture with generative adversarial networks. *Petroleum Science, 16*(3), 541–549. https://doi.org/10.1007/s12182-019-0328-4

Zhu, J. Y., Park, T., Isola, P., & Efros, A. A. (2017). Unpaired Image-to-Image Translation Using Cycle-Consistent Adversarial Networks. In *Proceedings of the IEEE International Conference on Computer Vision* (pp. 2223–2232). https://doi.org/10.1109/ICCV.2017.244

Appendices

A. GANSim

GANs includes two neural networks called generator (G) and discriminator (D) which are generally designed as CNNs. In GANs-based unconditional geomodelling (e.g., Song et al.,

(2021a)), given a number of training conceptual facies models, the discriminator and generator are alternatively trained by maximizing and minimizing a loss function given as

$$L(G_\theta, D_\varphi) = \mathbb{E}_{x_r \sim p_{data}}\left[logD_\varphi(x_r)\right] + \mathbb{E}_{z \sim p_z}\left[\log\left(1 - D_\varphi\left(G_\theta(z)\right)\right)\right], \quad \text{(A1)}$$

where, L is the GANs loss, θ and φ are the trainable parameters of G and D, p_{data} is the distribution of training facies models, x_r is one random sample of p_{data}, z is a low-dimensional latent vector, p_z is the distribution of z, and $\mathbb{E}$ is the expectation operator. After training, the generator learns spatial geological patterns from the training data and can thus map a random latent vector into a realistic facies model.

Compared to the GANs for unconditional geomodelling, GANSim (Song et al., 2021b, 2022a) has two features: first, the generator takes global features, well facies data, and facies probability maps as input conditioning data in addition to the original random latent vector; second, additional condition-based loss functions are introduced for the three types of input conditioning data. Figure A1 shows the architecture of the generator used for geomodelling of 2D channel reservoirs (Song et al., 2022a), which is also used in this paper (see section 3.1). The generator includes two types of pipelines: main pipeline as the backbone and input pipelines for the three types of input conditioning data. GANSim uses the progressive training approach where the generator and the discriminator are trained layer by layer (or block of layers by block of layers) from shallow, coarse resolution to deep, finer resolution (Karras et al., 2017). In the input pipeline of the facies probability map, the input probability map (64×64) is first downsampled into various coarser resolutions (e.g., 4×4, 8×8, etc.) and then converted into feature cubes with the same resolution (e.g., the feature cube with size of 4×4×16 and 8×8×16) through 1×1 convolutional kernels. Next, these feature cubes are concatenated with the feature cubes having the same size of the main pipeline. The input pipeline for the well facies data is the same as that of the probability maps. The global feature values are directly concatenated with the input latent vector, and their combination goes through all layers of the main pipeline. The architecture of the discriminator is basically symmetrical to the main pipeline of the generator (Song et al., 2022a).

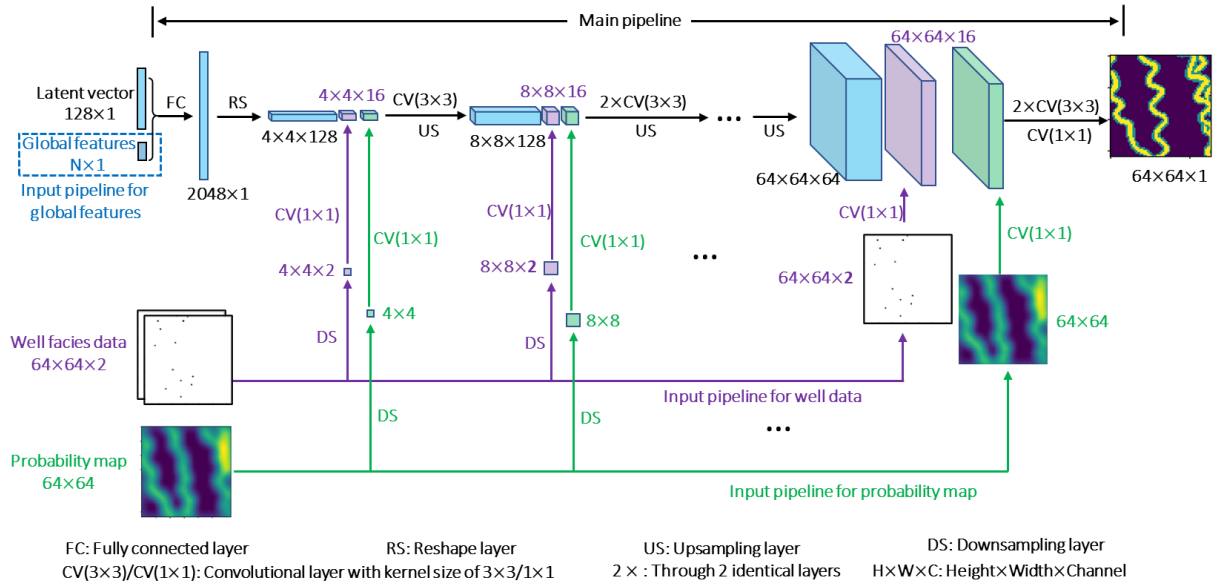

Figure A1. Architecture of the generator used for geomodelling of 2D sinuous channel reservoirs in GANSim framework, which is used in Song et al. (2022a) and this paper.

In GANSim, the condition-based loss function for the input global features is defined as

$$L(G_\theta)_g = \mathbb{E}_{z\sim p_z,(g,w,p)\sim p_{(g,w,p)}} \parallel f_g[G(z,g,w,p)] - g \parallel_2, \quad \text{(A2)}$$

where, g, w, and p represent input global features, well facies data, and probability maps, respectively, and $p_{(g,w,p)}$ is their joint distribution. Function f_g maps a generated facies model into its true global feature values, while $\|\cdot\|_2$ refers to the Euclidean L_2 distance. The condition-based loss function for the input well facies data is

$$L(G_\theta)_w = \mathbb{E}_{z\sim p_z,(g,w,p)\sim p_{(g,w,p)}} \parallel I_{wloc} \odot [G(z,g,w,p)] - w \parallel_2, \quad \text{(A3)}$$

where, I_{wloc} is the indicator of well locations, and $\odot$ is the element-wise product operator. The condition-based loss function for the input probability maps is

$$L(G)_p = \mathbb{E}_{z_1,z_2,\dots,z_m\sim p_z,(g,w,p)\sim p_{(g,w,p)}} \parallel f_p[G(z_1,g,w,p),\cdots,G(z_m,g,w,p)] - p \parallel_2, \quad \text{(A4)}$$

where, $z_1, z_2, \dots, z_m$ are random latent vectors sampled from p_z, and f_p calculates the frequency map for each facies type from the m generated facies models ($G(z_i,g,w,p), i = 1,\dots,m$) by calculating the percentage of each facies type at each point. Parameter m is a predefined hyperparameter. Each time when the generator is trained, a weighted combination of these condition-based losses and the GANs loss (Equation (A1)) is minimized to enable the generator to learn the relationship between the three types of input conditioning data and the output facies model as well as expected geological patterns, while when the discriminator is trained, only the GANs loss is maximized.

After training, the generator can produce reservoir facies models consistent with expected geological patterns (as represented in the training set) as well as the three types of input conditioning data. Changing the input latent vector values produces multiple different conditional reservoir realizations for uncertainty assessment. The three types of conditioning data are not necessarily always included, in which case the input pipeline and the condition-based loss of that excluded conditioning data are deleted.

References:

Karras, T., Aila, T., Laine, S., & Lehtinen, J. (2017). Progressive growing of GANs for improved quality, stability, and variation. *ArXiv Preprint*, arXiv: 1710.10196.

Song, S., Mukerji, T., & Hou, J. (2021a). GANSim: Conditional facies simulation using an improved progressive growing of Generative Adversarial Networks (GANs). *Mathematical Geosciences*. https://doi.org/https://doi.org/10.1007/s11004-021-09934-0

Song, S., Mukerji, T., & Hou, J. (2021b). Geological facies modeling based on progressive growing of Generative Adversarial Networks (GANs). *Computational Geosciences*. https://doi.org/https://doi.org/10.1007/s10596-021-10059-w

Song, S., Mukerji, T., & Hou, J. (2022). Bridging the gap between geophysics and geology with Generative Adversarial Networks (GANs). *IEEE Transactions on Geoscience and Remote Sensing*, *60*, 1–11. https://doi.org/10.1109/TGRS.2021.3066975

B. Latent vector search approaches

B.1 MCMC

Different MCMC variants have been developed (Brooks et al., 2011). In this study, we use a straightforward variant – Metropolis-Hastings framework.

We denote by d as the variable of geophysical or dynamic data and d^{obs} as the field measurement. MCMC aims to sample a series of latent vectors from the posterior probability distribution $p(z|d = d^{obs})$. Based on Bayes' rule, $p(z|d)$ is proportional to $p(z) \cdot p(d|z)$. Both the prior $p(z)$ and the likelihood $p(d|z)$ are assumed as Gaussian distributions: $p(z) \sim N(\mathbf{0}, \sqrt{C_Z})$, $p(d|z) \sim N(g(z), \sqrt{C_D})$, where N refers to a Gaussian distribution, C_Z and C_D are predefined covariance matrixes, and $g(\cdot)$ is the combined process of the pretrained generator and the pretrained surrogate. Basic steps of Metropolis-Hastings framework include

(1) randomly sample an initial latent vector z_0 from its prior distribution $p(z)$;

(2) inner loop:

- Step 1: randomly sample a new latent vector candidate z_1 based on a proposal distribution $p_{z_1|z_0}$ which is predefined as a Gaussian distribution centered at the current latent vector sample z_0;
- Step 2: calculate the probability to accept the candidate z_1: $\rho = \frac{p(z_1) \cdot p(d^{obs}|z_1)}{p(z_0) \cdot p(d^{obs}|z_0)}$;
- Step 3: based on ρ, determine whether candidate z_1 is accepted; if so, keep z_1 and replace z_0 with z_1.

After some burn-in initial iterations, the accepted latent vector samples approximately follow the posterior probability distribution $p(z|d = d^{obs})$ and are the appropriate latent vectors to be used as inputs to the GANSim-surrogate network. Multiple Markov chains may be performed to improve the variety of the samples, especially in a multi-modal posterior probability distribution.

B.2 Iterative Ensemble Smoother (IES)

IES, deriving from Ensemble Smoother methods, is commonly used for history matching (Evensen, 2018). It updates an ensemble of reservoir geomodels iteratively so that the ensemble gradually matches the given historical data. Here we use the Levenberg-Marquardt form of IES developed by Chen & Oliver (2013). As described in Appendix B.1, Both the prior $p(z)$ and the likelihood $p(d|z)$ are assumed as Gaussian distributions. The latent vector ensemble updating equation can be formulated as

$$z_{l+1,j} = z_{l,j} - \frac{1}{\lambda_l}\left[C_{Z_l Z_l} - C_{Z_l D_l}\left((1+\lambda_l)C_D + C_{D_l D_l}\right)^{-1} C_{D_l Z_l}\right] {C_z}^{-1}\left(z_{l,j} - z_j^{pr}\right) - C_{Z_l D_l}\left((1+\lambda_l)C_D + C_{D_l D_l}\right)^{-1}\left(g\left(z_{l,j}\right) - d_j^{obs}\right). \quad \text{(B1)}$$

In this equation, j is the latent vector index of the ensemble, z_j^{pr} is a sample from the prior, and d_j^{obs} is a sample from the Gaussian distribution $N\left(d^{obs}, \sqrt{C_D}\right)$. Parameter l denotes the iteration step, Z_l denotes the latent vector ensemble at the iteration step l, D_l is the ensemble of the

simulated geophysical/dynamic data calculated from Z_l through the combination of the pretrained generator and the pretrained surrogate (i.e., $g(\cdot)$), $C_{Z_l Z_l}$ is the covariance matrix of Z_l, $C_{Z_l D_l}$ is the cross-covariance matrix of Z_l and D_l, $C_{D_l D_l}$ is the covariance matrix of D_l, $C_{D_l Z_l}$ is the cross-covariance matrix of D_l and Z_l, and λ_l is a predefined hyperparameter. The initial ensemble of latent vectors are randomly sampled from the prior.

In cases of multi-modal posterior probability distribution, the finally obtained ensemble may converge to one of these modes, leading to a reduced diversity of the sampled latent vectors. Multiple rounds of IES program may be performed to alleviate this problem. Other variants of IES may also address this problem, e.g., the iterative local updating ensemble smoother proposed by Zhang et al. (2018).

B.3 Gradient descent

In the proposed GANSim-surrogate framework, when fixing the trained generator and the trained surrogate, the mismatch between the simulated and measured dynamic/geophysical data is purely a function of the input latent vector. The mismatch term can then be defined as a loss, and by minimizing the loss through gradient descent algorithm, the best latent vector consistent with the field-measured data can be found. Multiple runs of gradient descent with random starts result in different optimal latent vectors. It is worth nothing that the gradient descent approach cannot guarantee a globally minimal loss.

B.4 Gradual deformation

Gradual deformation was originally proposed by Hu (2000) and Hu et al. (2001) to search for the optimal reservoir model for history matching. Here, we specify it as follows to search for optimal latent vectors:

(1) sample a latent vector z_1 from the prior distribution $p(z)$;

(2) inner loop:

- Step 1: sample another latent vector z_2 from the prior distribution $p(z)$;
- Step 2: based on a variable r ($-\pi \leq r \leq \pi$), define $z' = z_1 \cos r + z_2 \sin r$, and find the optimal value r_{opt} so that the mismatch between the simulated data ($g(z')$) and the measure data is minimized;
- Step 3: replace z_1 with ($z_1 \cos r_{opt} + z_2 \sin r_{opt}$).

Similar to gradient descent, multiple rounds of gradual deformation program can be performed to obtain different appropriate latent vectors.

References:

Brooks, S., Gelman, A., Jones, G. L., & Meng, X. L. (2011). *Handbook of Markov Chain Monte Carlo*.. https://doi.org/10.1201/b10905

Chen, Y., & Oliver, D. S. (2013). Levenberg-Marquardt forms of the iterative ensemble smoother for efficient history matching and uncertainty quantification. *Computational Geosciences*. https://doi.org/10.1007/s10596-013-9351-5

Evensen, G. (2018). Analysis of iterative ensemble smoothers for solving inverse problems.

Computational Geosciences. https://doi.org/10.1007/s10596-018-9731-y

Hu, L. Y. (2000). Gradual deformation and iterative calibration of Gaussian-related stochastic models. *Mathematical Geology*. https://doi.org/10.1023/A:1007506918588

Hu, L. Y., Blanc, G., & Noetinger, B. (2001). Gradual deformation and iterative calibration of sequential stochastic simulations. *Mathematical Geology*. https://doi.org/10.1023/a:1011088913233

Zhang, J., Lin, G., Li, W., Wu, L., & Zeng, L. (2018). An Iterative Local Updating Ensemble Smoother for Estimation and Uncertainty Assessment of Hydrologic Model Parameters With Multimodal Distributions. *Water Resources Research*. https://doi.org/10.1002/2017WR020906